2021

Evaluation of Radiative Conductivity inside a Porous Media with the Effect of Participating Medium Based on Microscale Imaging

Mingping Zheng
University of Kentucky, zhengmingping@yahoo.com
Author ORCID Identifier:
https://orcid.org/0000-0001-7490-7930
Digital Object Identifier: https://doi.org/10.13023/etd.2021.299

STUDENT AGREEMENT:

I represent that my thesis or dissertation and abstract are my original work. Proper attribution has been given to all outside sources. I understand that I am solely responsible for obtaining any needed copyright permissions. I have obtained needed written permission statement(s) from the owner(s) of each third-party copyrighted matter to be included in my work, allowing electronic distribution (if such use is not permitted by the fair use doctrine) which will be submitted to UKnowledge as Additional File.

I hereby grant to The University of Kentucky and its agents the irrevocable, non-exclusive, and royalty-free license to archive and make accessible my work in whole or in part in all forms of media, now or hereafter known. I agree that the document mentioned above may be made available immediately for worldwide access unless an embargo applies.

I retain all other ownership rights to the copyright of my work. I also retain the right to use in future works (such as articles or books) all or part of my work. I understand that I am free to register the copyright to my work.

REVIEW, APPROVAL AND ACCEPTANCE

The document mentioned above has been reviewed and accepted by the student's advisor, on behalf of the advisory committee, and by the Director of Graduate Studies (DGS), on behalf of the program; we verify that this is the final, approved version of the student's thesis including all changes required by the advisory committee. The undersigned agree to abide by the statements above.

Mingping Zheng, Student

Dr. Alexandre Martin, Major Professor

Dr. Alexandre Martin, Director of Graduate Studies

Evaluation of Radiative Conductivity inside a Porous Media with the Effect of Participating Medium Based on Microscale Imaging

---

THESIS

A thesis submitted in partial fulfillment of the
requirements for the degree of Master of Science in
Mechanical Engineering in the College of Engineering
at the University of Kentucky

By
Mingping Zheng
Lexington, Kentucky

Director: Dr. Alexandre Martin, Professor of Mechanical Engineering
Lexington, Kentucky 2021

https://orcid.org/0000-0001-7490-7930

ABSTRACT OF THESIS

Evaluation of Radiative Conductivity inside a Porous Media with the Effect of Participating Medium Based on Microscale Imaging

Space vehicles will experience high loads of heat while entering planetary atmosphere. At such high temperature, radiation becomes the dominant mode of heat transfer. Since the atmospheric entry enviroment is nearly impossible to duplicate in a laboratory environment, a numerical model to evaluate thermal performance of the thermal protection system was established. The model simulates the radiative heat transfer process in highly porous media, and the process also takes into account the influence of the participating media.

KEYWORDS: thermal protection system, fibrous material, effective radiative conductivity, participating medium, porous media, numerical model

Author's signature: Mingping Zheng

Date: July 31, 2021

Evaluation of Radiative Conductivity inside a Porous Media with the Effect of Participating Medium Based on Microscale Imaging

By

Mingping Zheng

Director of Thesis: Alexandre Martin

Director of Graduate Studies: Alexandre Martin

Date: July 31, 2021

Dedicated to my family.

ACKNOWLEDGMENTS

First and foremost, I would like to express my deepest gratitude to my advisor Dr. Alexandre Martin, for his continuous support during course of my master. His immense knowledge and profound experience have encouraged me all the time during my academic journey. He was patient with me throughtout my master. He always can provide insigful comments when I stuck. When I was in the rock bottom during this epidemic crisis, he guided me out step by step. Without his guidance and encouragement, I will not be able to persist in completing this study.

Beside my advisor, I would like to offer my special thanks to Dr. Beck and Dr. Tagavi for their insightful comments and suggestions about radiation modeling. I would like to thank all the members in the committee: Dr. Savio Poovathingal and Dr. John Maddox.

Additionally, I would like to express my sincere thanks to all my colleagues at the Gas Surface Interactions Lab: Rick Fu, Sean McDaniel, Raghava Davuluri, etc. Thank you all for selfless supports, encouragements, and random chats that made the time at the lab full of vitality. I also want to extend my thanks to Nima Nouri for his original contribution to this study.

Lastly, I would like to thank my parents, grandparents, and my cousins for always being there with unconditional love and support. I would also like to offer my special thanks to Kim for her love and emotional support. I am deeply grateful for all the loves that I have received.

CONTENTS

LIST OF TABLES

LIST OF FIGURES

Chapter 1 Introduction

1.1 Background

Mankind has always been fascinated by the mysteries of the universe, and rapid development of space exploration is a recent example of this interest. Human migration to other planets is no longer science fiction, it is becoming a reality. Numerous missions range from exploring celestial bodies, collecting dust samples from a comet, and retrieving astronauts from the International Space Station (ISS). Vehicles required for these missions are designed to satisfy a set of requirements to fulfill specific goals, and atmospheric entry serves as one of the most demanding phases among these missions. Re-entry is the movement of an object returning to the planet from outer space through the atmosphere. This phase of a mission usually has three main requirements: deceleration, heating, and accuracy of landing. Furthermore, re-entry process of a spacecraft usually consists of three stages: entry, descent, and landing, which is commonly referred to as EDL. When a vehicle entering the atmosphere of the planet, it needs to survive a series of harsh conditions. First, the vehicle is moving at hypersonic speeds and it is maneuvering to land on a specific location. At such high velocity interaction with the atmosphere, the kinetic energy of the vehicle is being dissipated mainly in the form of heat. Although most of the heat is released to the surrounding by radiation and convection, a fraction still remains on the surface and causes severe temperature increase. The temperature at the surface could reach several thousands of Kelvin. At such high temperature, radiation becomes the dominant mode of heat transfer. Furthermore, the chemical reactions between the pyrolysis gases and the thermal boundary layer exacerbated the temperature rise. In order to ensure that the human or fragile payload inside the vehicle survives such high temperatures, a Thermal Protection System (TPS) is needed for the atmospheric

entry vehicle. TPS can counter the high heat flux by absorbing, radiating it to surroundings, and provide safety to the payload or human inside the vehicle. TPS is a critical component for any atmospheric entry vehicle, and the future potential of the spacecraft at a more demanding environment will depend upon the capabilities of the TPS. Figure 1.1 depicts the artistic interpretation of atmospheric entry for SpaceX Dragon capsule.

Figure 1.1: SpaceX dragon capsule entering the atmosphere of Earth (Courtesy of SpaceX [4])

Various types of Thermal Protection Systems have been investigated through past research and developments: the Radiative System [7], Heat-Sink System [22], Transpiration and Film Cooling System [[25], [14]], Convective Cooling System [12], and Ablative System [45]. For planetary exploration, ablative TPS are most widely used, because of their excellent performance, light weight, and reliability. For the ablative heat shield, carbon is often used due to its properties: good heat sink and radiation properties, high melting point, and relatively light weight. Ablative materials mitigate

the transfer of energy to thermal by a mechanism called ablation. This phenomenon is loosely defined as the removal of mass through energy transfer processes. An ideal ablative material can dispose of large amounts of heat with only a minor amount of material loss. As the surface burns and dissipates thermal energy into space, the remaining solid material continues to insulate the heat from the outside environment and maintain the vehicle at a safe termperature. Hence, appropriate thickness of the ablative material is necessary for the vehicle to survive entry conditions during a mission [3].

Phenolic Impregnated Carbon Ablator (PICA) was first developed by NASA Ames in the 1980's as the heat shield for the Stardust capsule. As a new generation of light weight fibrous ablative heat shield, PICA demonstrated excellent performance at high heat fluxes. These materials are made with phenoic resin and carbon subtrate called FiberForm. PICA has proved to be effective and reliable when subject to high heat flux by many of the modern spacecraft including the Stardust mission and the SpaceX Dragon Capsule [41].

Figure 1.2: Stardust capsule after successfully landing (Courtesy of NASA [13])

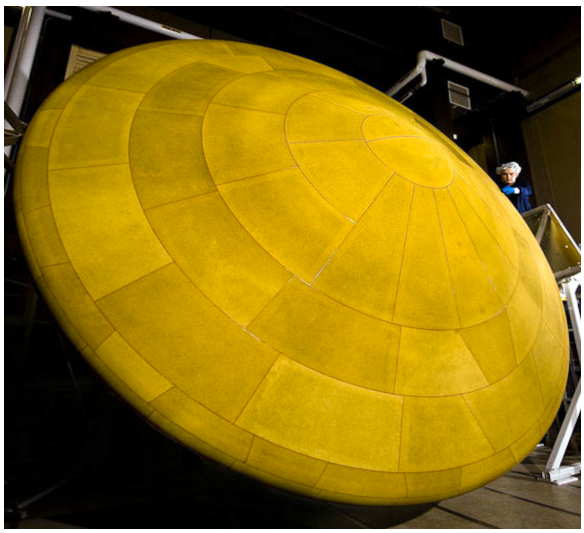

Figure 1.3: PICA heat shield from Mars Science Laboratory (MSL) (Courtesy of NASA [20])

To better understand the performance of PICA at a microscopic scale, and how the microscale structures affect the material properties, a radiation exchange model is developed to extract the effective radiation conductivity based on microscale samples. This understanding could lead to more comprehensive modeling of the thermal transport through the porous media, and provide insight for creating a more effective heat shield in the future.

Numerical models were used to study the radiation heat transfer process with both artificial geometry and a real microscale sample. Additionally, radiation through absorbing-emitting gas was investigated. As radiation passes through a gas, its intensity will be reduced due to absorption and scattering. Accounting for the gas effect will improve the fidelity of the model for radiation through porous media. In this work, numerical simulations were performed using a FiberForm microstructure. Stastical analysis was used to investigate the distribution of thermal conductivity among artificial FiberForm samples. Ultimately a deeper knowledge of the microscale radiative heat transfer can lead to more efficient and reliable thermal protection systems in the future.

1.2 Thermal radiation

Heat is a form of energy which can be transferred by a system interacting with its surrounding. There are two modes of heat transfer: conduction and radiation. The consensus usually adds convection as the third mode of heat transfer, but it is essentially conduction plus advection. Thus, only conduction and radiation will be discussed in this chapter.

1. Conduction

   Conduction occurs when two objects with different temperatures are in direct contact with each other. The govening equation for conduction heat transfer is

Fourier's law:

$$\dot{Q}_{cond} = -kA\frac{dT}{dx} \tag{1.1}$$

where $\dot{Q}_{cond}$ is the rate of conduction heat transfer, k is the material thermal conductivity, A is area of the surface, and dT/dx is the temperature gradient in the direction of heat transfer. Conduction occurs more readily in solids and liquids, since the particles are closer together. The rate of conduction heat transfer is higher when the temperature difference is large.

2. Radiation

Radiation transferred the thermal energy with electromagnetic waves emitted by atomic and subatomic agitation at the surface of a body [47]. The energy radiated by a black surface is given by the Stefan-Boltzmann Law:

$$\dot{Q}_{rad} = \sigma\, A\, T^4 \tag{1.2}$$

where $\dot{Q}_{rad}$ is the rate of radiation heat transfer, σ is the Stefan-Boltzmann constant, A is the surface area of the radiator, and T is the temperature of the surface. The term black represents an ideal surface that absorbs all incident radiation and reflects none. Real bodies radiate less effectively than black bodies. Radiation travels at the speed of light and it does not require an intervening medium to transmit. Hence, radiation is the only possible mode for heat transfer in a vacuum.

Radiation is a vitally important mode of heat transfer, the existence of life depends on the solar radiative energy incident upon Earth. Radiation can be viewed as propagation of electromagnetic waves. All forms of matter emit electromagnetic radiation constantly. Since radiation is a consequence of kinetic energy fluctuations of the atoms, any objects with temperature greater than

absolute zero will emit radiation to the surrounding environment. The energy of radiation depends on the wavelength and it varies over a wide range. However, only a limited portion can be directly detected by the human eye. Human eyes are only sensitive to radiation wavelengths approximately ranging from 0.4 to 0.7 μm, which is called the visible spectrum. Thermal radiation only occurs on a narrow band approximately from 0.1 to 100 μm, which includes a portion of the Ultraviolet(UV), all the visible and infrared (IR) regions, as illustrated in Fig. 1.4.

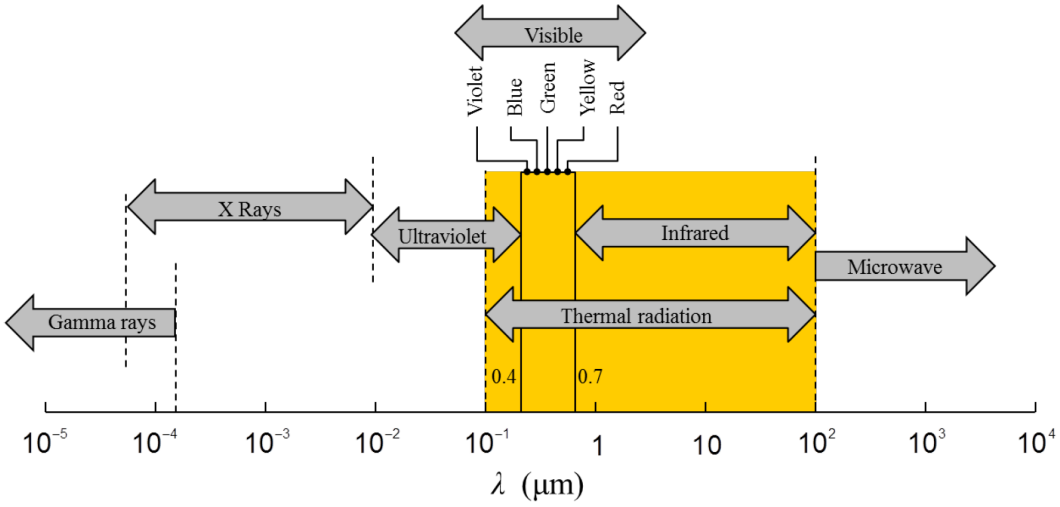

Figure 1.4: Spectrum of electromagnetic radiation, where the thermal radiation is highlighted in yellow region (Courtesy of Baudouy) [2])

Another distinguishing feature for radiative heat transfer is the fourth order absolute temperature dependence $\mathcal{O}(\Delta(T^4))$. For conduction, the transfer energy depends on the differences between temperature approximately at first order $\mathcal{O}(\Delta(T))$. Thus, the importance of radiation is amplified at high temperatures. Radiation contributes substantially during the atmospheric entry process due to high temperatures at contacting surface. The first law of thermodynamics states that total energy is conserved in a closed system. The kinetic energy of

the gas particles during atmospheric entry is primarily converted into thermal energy, and the thermal energy developed from the aerodynamics heating process is mostly re-radiated back into space or carried away to the surroundings by convection.

1.3 Past research on radiative heat transfer models

Radiation is an essential mode of heat transfer that must be considered in high temperature applications. The rapid advancement of these applications ranging from rocket engines, heating furnaces, nuclear reactors, material processing, atmospheric entry vehicles, etc, have provided compelling impetus for further study in the area of radiative heat transfer. In these applications, the heat transfer rate is significantly influenced by radiation; therefore, it is crucial to understand radiation and develop practical numerical models to simulate real-life engineering problems. For a static compressible fluid, the thermal energy conservation equation is given as:

$$\rho\, c_p \frac{\partial T}{\partial t} = -\nabla \cdot (-k\nabla T + q_r) \tag{1.3}$$

In Eq. 1.3, the terms from left to right represent local energy change in time, conduction, and radiation. Although radiation q_r is part of the heat flux terms from the equation above, it is the most challenging part to calculate, especially in the presence of participating media. Thus, the radiation q_r is usually lumped into the conduction terms and evaluated independently from the radiative transfer equation (RTE).

Since radiation is critical in high-temperature applications, numerous simulation models have been developed from past researchers. Determining the radiative heat transfer in porous media is a highly complex problem. The complexity makes the complete solution a formidable task, even with supercomputers. The radiation exchange model has continued to evolve to be more efficient and accurate. A couple of models related to this research will be discussed here, along with their advantages and disadvantages when dealing with porous media problems.

1. Rosseland radiation model

In 1931, Rosseland [38] provided an approximation for the net radiation heat flux with optically thick media, and the equation is given as follow

$$q_r = -\frac{4}{3a_R}\nabla(e_b) \tag{1.4}$$

where a_R is the Rosseland mean extinction coefficient, where the participating medium can absorb, emit, and isotropically scatter the radiation. e_b is the black body emission and is given by Stefan's Law from Eq. 1.2. From the problem between two plane surfaces with a grey medium between, where grey represent the emissivity is independent of wavelength, Eq. 1.4 is reduced to,

$$q_r = -\frac{16\sigma}{3a_R}T^3\frac{dT}{dx_i} \tag{1.5}$$

where x_i is the direction normal to the surface. Together with Eq. 1.3, the effective thermal conductivity is defined as

$$k_{eff}(T) = k(T) + \frac{16\sigma}{3a_R}T^3 = k_c + k_r \tag{1.6}$$

where k_c is the solid conductivity and k_r is the radiative conductivity. And the energy balance equation from Eq. 1.3 can be written with the following form

$$\rho\, c_p\frac{\partial T}{\partial t} = -\nabla\cdot(-k_{eff}\nabla T) \tag{1.7}$$

Thus, the Rosseland diffusion approximation is also referred to as radiative conduction approximations, and Fourier's law can be used to extract the effective radiative conductivity with good accuracy. Viskanta and Grosh [46] utilized the Rosseland approximation to solve the boundary layer heat transfer problem over a wedge geometry. Cess [5] investigated the interaction between radiation and conduction. Hossain [17], [18] studied the effect of radiation in free convection flow over porous vertical plates with the variation in viscosity. Malek et al. [27] first applied the Rosseland model to non-grey optically thick media using enriched basis functions. Mendes et al. [29] evaluated the effective

thermal conductivity of open-cell foam-like structures based on the Rosseland approximation.

The Rosseland approximation is a convenient way to solve the radiation conduction problem by grouping the radiation terms in some modified transport coefficients. The radiative conductivity term can be obtained separately using another approach and conjugate with the Rosseland approximation. The major limitation for the Rosseland model is that it can only be used for optically thick media [26]. In addition, direction dependence properties like anisotropic scattering are not compatible with the Rosseland approximation.

2. Net radiation method

Net radiation method is formulated based on the surface to surface radiation exchange relation. The numerical model developed from this research is based on the direct exchange factor approach. Thus, only a basic introduction is given in this section and more details about the method will be discussed later on.

The net rate of radiation leaving surface i is defined as the difference between outgoing radiation J_i and incident radiation G_i,

$$Q_i = A_i(J_i - G_i) \tag{1.8}$$

where J_i and G_i are also referred to as radiosity and irradiation, respectively. The radiosity is composed of emitted plus reflected radiation leaving the surface such that

$$J_i = A_i(e_i - \alpha_i G_i) \tag{1.9}$$

where e_i is the black body radiation, and α_i is the absorptivity. This method is widely used for the surface radiation exchange problem. Kang et al. [24] studied the radiation through Porous Media of Inorganic Intumescent Coating using equations derived from the net radiation method. He also simulated the combined conduction-radiation transfer based on the Rosseland approximation and studied the effect of porosity on thermal conductivity.

Van Eekelen and Lachaud [44] validated the effective radiation heat transfer model for two dimensional Fiber Preforms geometry based on net radiation method and Rosseland approximation. Fan et al. [11] analyzed the combined radiation conduction problem in open-cell metallic foam based on tomographic reconstruction geometry.

Nima [31], [32], [33] used the net radiation method and Rosseland approximation to evaluate the thermal performance of three dimensional fibrous insulators. In his work, the combined value of radiative and solid conductivity are compared to experimental data and showed excellent agreement. The contribution of solid and radiative conductivity in the overall heat transfer process is also highlighted. For temperatures lower than 650 K, the radiative conductivity can be neglected. And if the temperature is above 3000 K, the radiation dominates conduction and solid conductivity can be neglected [33]. The original formulation of net radiation method is unable to consider the effect of participating media; thus, the result from Nima only occurs in vacuum regimes.

This research is a direct extension of the work from Nima. The solution to unbalance heat flux has been introduced. In addition, a participating medium that can absorb and emit radiation is considered in the model. Statistical analysis was performed over 35 samples of artificial FiberForm, and the transverse isotropic property was emphasized. Although the result lacks verification from the actual engineering experiment, the numerical model can simulate the radiative exchange process at a microscale level and contribute to the understanding of radiation through porous media.

3. Zonal Method

In real life engineering problems, the zonal method is one of the most commonly used approaches for calculating the radiative heat exchange process. This method was first established by Hottel and Cohen [19] in 1958. They

divided a furnace system into surface zones and gas zones, and each zone was characterized by uniform radiative properties and temperature distribution. By evaluating the direct radiation exchange between zones and implementing into energy balance equations, the radiation heat flux over the surfaces can be determined. The radiant interchange between zones requires the determination of matrices of corresponding radiative-exchange factors, and these exchange factors may be precomputed if the surface and gas properties are temperature independent. The net radiation heat for the surface zone i can be described by [9],

$$Q_{rad,i} = \sum_{j=1}^{Ns} \overrightarrow{S_i S_j} E_{s,j} + \sum_{k=1}^{Ng} \overrightarrow{S_i G_k} E_{g,k} - A_i \epsilon_i E_{s,i} \tag{1.10}$$

where $E_{s,j}$ and $E_{g,k}$ represent the emitted energy from surface j and gas volume k. $\overrightarrow{S_i S_j}$ is the directed flux area from surface i to surface j, and $\overrightarrow{S_i G_j}$ is the total exchange area between gas zone j and surface zone i. The equations for the Zonal method are similar to the net radiation method that Nima used, except that the gas terms are included. The gas in the Zonal method is treated separately by defining a volumetric zone. Between gas and surface zone, the total radiation exchange process can be categorized into four different cases [8]:

a) Surface zone to surface zone

b) Surface zone to gas zone

c) Gas zone to surface zone

d) Gas zone to gas zone

This method has been extended to more complicated cases. Eckert [10] expands the analysis into non-constant and non-grey absorption coefficients. H. F. Nelson [15] applied this method with an optically thick medium and verified it with experimental results. In 1994, Yuen and Takara [48] modified the zonal method on a radiative transfer problem with absorbing and anisotropically scattering

media inside a cubic enclosure. ZHANG et al. [49] have simplified the zonal method for radiation calculation inside a furnace by introducing the imaginary planes in 2014.

The zonal method is very accurate if the inputs parameters are sufficiently precise and the model volume is divided into sufficiently small portions. However, one of the major limitations for the Zonal method is its capability to deal with complex geometry. The number of zones increases rapidly when subjecting to irregular geometry like porous media. Therefore, substantial memory and computational cost will be required to solve a big dense matrix of exchange factors. Thus, the Zonal method is not ideal when dealing with radiation through porous media. Additionally, the Zonal method is unable to deal with anisotropic scattering, and results from the Zonal method are often inaccurate for optically thick media [30].

Chapter 2 Geometry Configuration Factor (GCF)

One of the important aspects of radiation heat exchange is the geometry configuration factor (GCF), also called view factor. It is defined as the fraction of the radiation leaving one surface that stikes another surface. View factor is purely a geometric parameter that also accounts for the orientation between two surfaces. A common example for view factor is the portion of radiation Earth receives compared to the total irradiance the Sun emits. The view factor will become large if two objects are closer together. In the calculation of view factor, the radiation is assumed to be uniform across the surface in all directions. Additionally, the participating medium is not involved in the calculation of view factors; post-processing is required in the presence of gas.

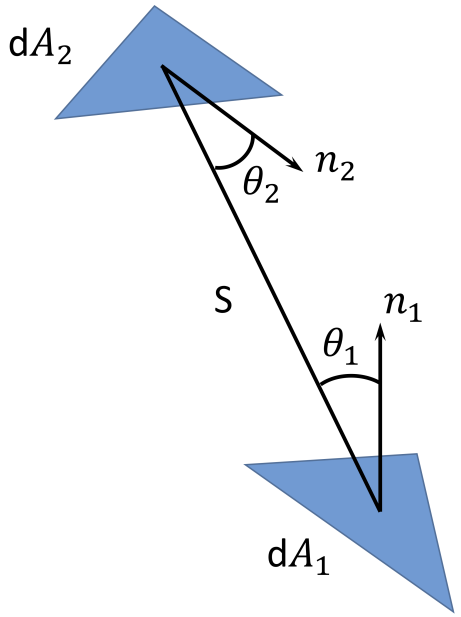

Figure 2.1: View factor for two differential area schematic.

2.1 The View Factor Integral

From the above definition of view factors, the explicit geometric dependence is given as follows: Consider arbitrarily oriented surfaces A_1 and A_2 separated by a distance S as shown in the Fig. 2.1, where n is the vector normal to the surface, and θ is the angle between the normal vector n and the line connecting the centroid between two surfaces. The view factor from surface dA_1 to dA_2 is defined as [34],

$$dF_{dA_1-dA_2} = \frac{\text{Energy leaving } dA_1 \text{ directly toward and intercepted by } dA_2}{\text{Total energy leaving } dA_1} \tag{2.1}$$

To derive the view factor equation between differential areas, the concept of radiation intensity I is used. Radiant intensity is defined as the amount of radiation heat flux that is transmitted, reflected, emitted, or received per unit angle. Mathematical treatment of radiation intensity usually requires the use of a spherical coordinate system. Here, a single wavelength, the radiation energy emitted and reflected from surface i in the direction (θ, ϕ) is considered, and given by,

$$I_{e+r,i}(\theta, \phi) = \frac{dq_{i-j}}{dA_i \, cos\theta_i \cdot d\omega_i} \tag{2.2}$$

hence, the rate at which radiation leaves dA_1 and intercept with dA_2 can be expressed as,

$$dq_{1-2} = I_1 \, cos\theta_1 \; dA_1 d\omega_1 \tag{2.3}$$

where I_1 is the intensity of radiation leaving surface 1 by reflection and emission., $d\omega_1$ is the differential solid angle subtended between dA_1 and dA_2, and can be written as:

$$d\omega_1 = \frac{cos\,\theta_2 \, dA_2}{S^2} \tag{2.4}$$

where S is the length of the line connecting the centroid between two surfaces, and θ_1 is the angle between the normal of surface 1 and S joining the two surfaces. Substituting $d\omega_1$ from Eq. 2.4 into Eq. 2.3 will obtain,

$$dq_{1-2} = I_1 \frac{cos\theta_1 \, cos\theta_2}{S^2} dA_1 \, dA_2 \tag{2.5}$$

The total radiative energy leaving dA_1 (radiation flux) is referred to as radiosity and can be related to intensity as $J = \pi I$. Therefore, the total radiation leaving surface 1 and intercepted by surface 2 can then be obtained by evaluating the integral:

$$q_{1-2} = J_i \int_{A_1} \int_{A_2} \frac{cos\theta_1 \, cos\theta_2}{\pi S^2} \, dA_2 \, dA_1 \tag{2.6}$$

The radiosity is assumed to be uniform over the surface. Since view factor is the fraction of the radiation that leaves one surface and reaches the other surface,

$$F_{1-2} = \frac{q_{1-2}}{A_1 J_1} \tag{2.7}$$

Together the expression for the view factor F_{1-2} is given by,

$$F_{1-2} = \frac{1}{A_1} \int_{A_1} \int_{A_2} \frac{cos\theta_1 \, cos\theta_2}{\pi S^2} \, dA_2 \, dA_1 \tag{2.8}$$

Similary, the view factor F_{2-1} is

$$F_{2-1} = \frac{1}{A_2} \int_{A_2} \int_{A_1} \frac{cos\theta_1 \, cos\theta_2}{\pi S^2} \, dA_1 \, dA_2 \tag{2.9}$$

The $cos\,\theta$ can be calculated using the cosine formula

$$cos\,\theta = \frac{\vec{v_1} \cdot \vec{v_2}}{\|\vec{v_1}\| \, \|\vec{v_2}\|} \tag{2.10}$$

where $\|\vec{v}\|$ represents the norm of the vector. The general expression for view factor between two isothermal and opaque surfaces has been obtained. Next, this relation is applied to different scenarios within the model.

2.2 GCF calculation

To evaluate the double area integral, a large surface needs to decompose into smaller sections to obtain accurate results. In the numerical model, the microscale geometry is composed of triangular surface elements. In addition, an imaginary boundary wall that bounds the geometry inside is required. The heat flux at the boundary walls provides information about the amount of radiation through the system in different

directions. For an three dimensional object, total of 6 boundary walls will be defined. Discretization is needed to accurately determine the view factor for the wall. The internal enclosure surfaces are thus discretized into smaller mesh areas as shown in the Fig. 2.2. One important thing to note, the boundary wall is usually desired to be close to the input geometry while maintaining an appropriate distance, so the view factor result is still robust. Therefore, good engineering judgment or boundary distance independent study might be needed depending on the problem.

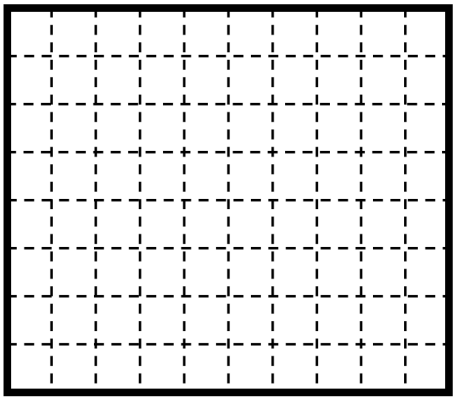

Figure 2.2: Illustration of the square mesh at the boundary wall for view factor calculation.

With the discretized square from the enclosure surface, and the triangles from the input geometry sample, 3 different cases of GCF calculation are presented.

1. Triangle - Triangle GCF calculation

   The GCF from one triangle surface to another can be obtained by directly solving Eq. 2.8. Thus, the fraction of energy leaving surface a_i that reaches the second surface a_j is given by,

$$F_{ij} = \frac{cos\theta_i \, cos\theta_j}{\pi S_{ij}^2} \, a_j \tag{2.11}$$

Where a_j is the area of surface j, and θ is the angle between the norm of the surface and the line S that connects the two triangle centroids.

2. Triangle to Internal enclosure surface GCF calculation

   Consider surface i as triangle surface and surface j as internal enclosure surface. Since the internal enclosure is composed of a dense square mesh. By taking out the integration for surface i, Eqs. 2.8 and 2.9 become

$$F_{ij} = \int \frac{cos\theta_i \, cos\theta_j}{\pi S_{ij}^2} \, dA_j, \tag{2.12}$$

$$F_{ji} = \frac{a_i}{A_j} \int \frac{cos\theta_i \, cos\theta_j}{\pi S_{ij}^2} \, dA_j. \tag{2.13}$$

   In the discretized form with uniform mesh grid area Eq. 2.12 becomes,

$$F_{ij} = \frac{\Delta A}{\pi} \sum_j \frac{cos\theta_i \, cos\theta_j}{S_{ij}^2} \tag{2.14}$$

   Where ΔA is the area of the discretized surface. Note that the accuracy of the view factor might be affected by the mesh resolution. Therefore discretized surface with at least two orders of magnitude smaller than the enclosure surface is used to ensure mesh independent results.

3. Internal enclosure surface to Internal enclosure surface GCF calculation

   Lastly, for the case of an internal enclosure surface to another internal enclosure surface. Since both surfaces have finite areas, the equation for view factor can be rewritten into discretized form as,

$$F_{ij} = \frac{(\Delta A)^2}{\pi A_i} \sum_{i,\,j} \frac{cos\theta_i \, cos\theta_j}{S_{ij}^2} \tag{2.15}$$

   Subscripts i and j refer to i^{th} and j^{th} subsurface and A_i is the area for the internal enclosure surface i.

In summary, the view factor equations for the 3 cases are shown in Table 2.1

Table 2.1: Summary for equations of geometric configuration factor

Case	Geometric configuration factor F_{ij}
1	$\frac{cos\theta_i \, cos\theta_j}{\pi S_{ij}^2} \, a_j$
2	$\frac{\Delta A}{\pi} \sum_j \frac{cos\theta_i \, cos\theta_j}{S_{ij}^2}$
3	$\frac{(\Delta A)^2}{\pi A_i} \sum_{i,\,j} \frac{cos\theta_i \, cos\theta_j}{S_{ij}^2}$

2.3 View Factor Properties

Usually, for an enclosure consisting of N surfaces, the arithmetic operation for the view factor calculation is approximately $\mathcal{O}(N^2)$. However, evaluating all of the view factors is unnecessary. Numerous arithmetic operations are saved by using some basic properties of view factors,

1. Reciprocity relations

   One of the most important properties of view factors is the reciprocity relations. Between two finite surfaces, the reciprocity relations is given by

   $$A_i F_{ij} = A_j F_{ji} \tag{2.16}$$

   Similarly, the reciprocity relation between differential area and finite area can be obtained from Eqs. 2.12 and 2.13.

   $$a_i F_{ij} = A_j F_{ji}, \tag{2.17}$$

   where a_i is the triangle area for and A_j is the area for the boundary surface j. Lastly, the reciprocity relation from two elemental areas takes the form

   $$a_i F_{ij} = a_j F_{ji} \tag{2.18}$$

   Reciprocity is a highly useful relation for the calculation of view factors. It states that the view factor ratio between two surfaces is inversely proportional

to the ratio between the area of two surfaces. By using this relation alone, half of the computational cost is saved since the view factor F_{ij} can be determined with the knowledge of F_{ji}.

2. Obstruction

   Two surfaces are able to exchange radiation if and only if they can view each other. This condition is reinforced by a subroutine in the code call ray fiber intersection test. If the line-of-sight (the line connecting two centroids of the surface) between two surfaces is blocked by another opaque object, the radiation interchange is prevented, and the view factor is automatically set to 0. In some cases, the radiation could be partially blocked since some portion of the surface is still able to view the other object. Since only the line-of-sight is considered, these cases are regarded as either fully blocked or non-blocked at all. By having a large number of triangle elements, this discrepancy is assumed to be negligible since the two situations will neutralize each other. Additionally, using a higher resolution mesh can also reduced the partially blocked errors.

3. Bounding

   In general, the view factor should always be bounded between 0 and 1 ($0 < F_{ij} < 1$). View factor of 0 represent two surfaces cannot see each other; and view factor of 1 means one surface completely enclosed by a second surface. Due to the numerical error, it is possible to obtain a view factor that is higher than 1. When the surface is extremely closer to another, a finer discretization is needed to ensure this condition is satisfied. A finer mesh on the boundary wall can prevent the violation of bounding property, but this will result in higher computational costs. If the triangular elements violated the bounding relation, the triangle will be subdivided into smaller triangle surface elements, and re-evaluate the view factor using the discretized equations.

4. Closeness

The sum of the view factor from a given surface should approximately equal 1 within an enclosure volume, where

$$\sum_{j=1}^{n} F_{ij} = 1 \tag{2.19}$$

This relation is important for the conservation of radiation energy within the enclosure because the same amount of radiation emitted by a surface must be absorbed. However, this is not always the case. Due to the numerical deviations from discretization and imprecision in the calculation of partial views, the summation could be slightly larger or smaller than 1.

To counter this numerical error, a normalization on the view factor is performed. This step is critical for the view factor calculation. If the sum of view factors for a given surface inside the enclosure is not exactly 1, problems will occur for the radiation exchange model due to the non-compact value. This will result in unbalanced energy due to leak or gain from the closeness problem of the view factor. Normalization can help eliminate this problem. It is accomplished by summing all the view factors for a given surface and then divide each associate view factor by this total value. This minor correction ensures the unity property of view factors, and is necessary for the radiation exchange model discussed later.

2.4 View Factor Validation

To verify the accuracy of the view factor calculation, a simple 3-D geometry is simulated with two perpendicular cylinders, as shown in the Fig. 2.3. The analytical approximate solution is given in [1] with the following expressions:

$$\begin{aligned} F_{1-2} &= 0.178(X/2.59)^{-0.95}\,(L/X)^{-0.16}\,\exp\left(-0.537\left|\ln(L/X)\right|^{1.61}\right) \qquad if\ L/X < 1 \\ F_{1-2} &= 0.178(X/2.59)^{-0.95}\,(L/X)^{-2.32}\,\exp\left(2.024\left|\ln(L/X)\right|^{0.889}\right) \qquad if\ L/X > 1 \end{aligned} \tag{2.20}$$

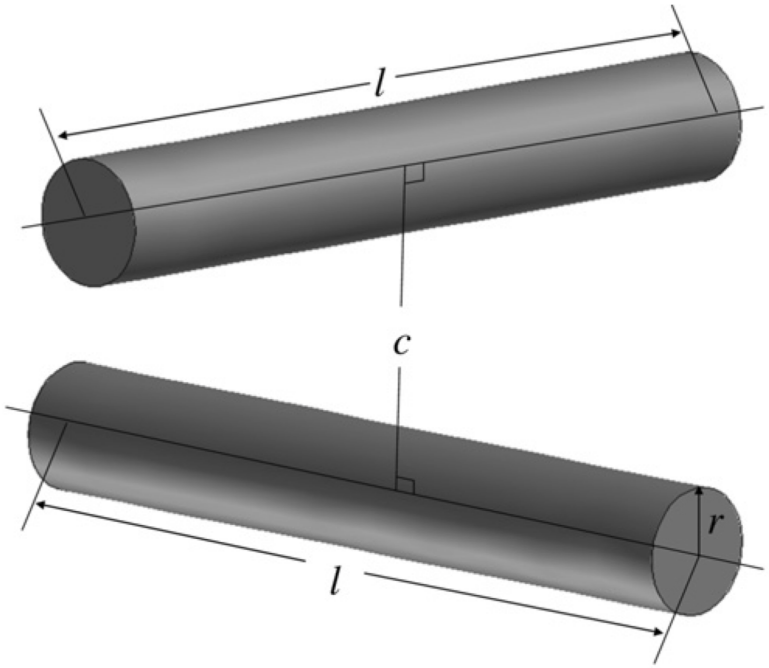

Figure 2.3: Verification test case of the view factor using two perpendicular cylinders [43]

Where $L = l/r$, $C = c/r$, and $X = 2.42C - 2.24$. In order to obtain the view factor between two cylinders, two fibers were created and discretized into triangular meshes, as shown in the Fig. 2.4. Case 1 from Table 2.1 is applied to obtain the view factor from triangle to triangle. Since the two cylinders in the test case have the same dimensions and the fibers cannot view themselves, the view factor between two cylinders can be simplified into the following relation:

$$F_{f1-f2} = F_{f2-f1} = \frac{1}{2A_f} \sum_{i,j} F_{ij} \, A_{ij} \tag{2.21}$$

where A_f is the surface area for one fiber. In general, the accuracy depends on the mesh resolution, but higher resolution also resulted in higher computational cost. Hence, it is important to study the impact of mesh resolution to determine the optimal level of discretization to be used. A mesh convergence study was performed to ensure the results are independent of the resolutions. The influence of the mesh resolution

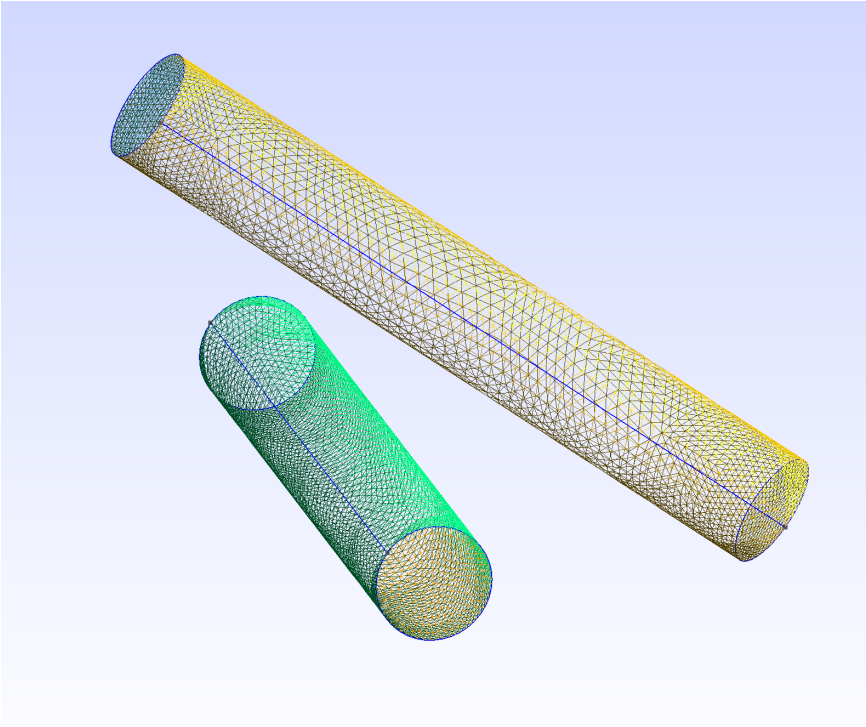

Figure 2.4: Illustration of the discretize mesh of the verification test case using two perpendicular cylinders

(number of triangles) was plotted in the Fig. 2.5. The parameters values used were $l = 200\,\mu m$, $c = 50\,\mu m$, and $r = 15\,\mu m$. The results show that 10,000 triangles were sufficient to generate mesh independent results for the two fibers problem. As for the result, our simulation predicted a value of 0.063, which has a close agreement with the analytical approximation value of 0.066. Figure 2.6 plotted the view factor as a function of the distance between two fibers using around 10,000 triangles in total. In this graph, the blue line is the analytical approximation from Eq. 2.20, and the red dot is the discretized solution. The view factor decreases as the distance between two fibers increases. Results from the discretize method are slightly lower than the analytical approximation, but an almost identical pattern is observed. Overall good agreement is obtained between the two approaches, with the largest difference at less than 5%. With this level of mesh refinement, the numerical result is anticipated to be more accurate than the analytical approximation.

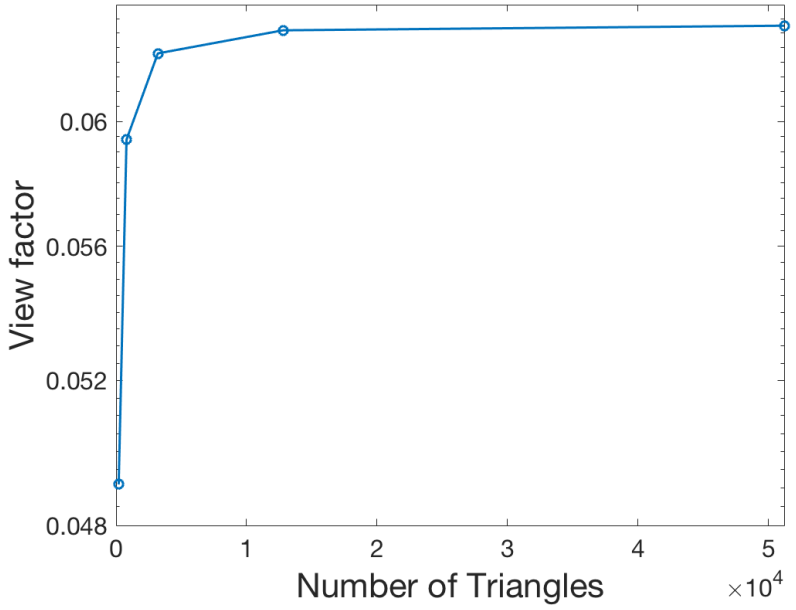

Figure 2.5: Mesh convergence study for the verification test case using two perpendicular cylinder test case ($c = 50$, c is the distance between two fibers)

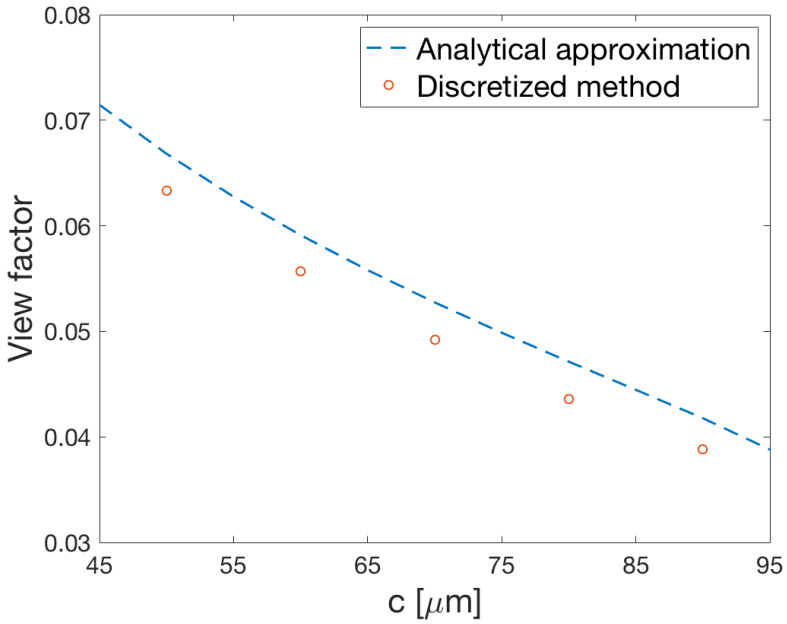

Figure 2.6: Comparison of configuration factors for two perpendicular cylinders as function of distance between cylinders, the analytical approximation is given by [1]

Chapter 3 Radiation conductivity and participating media

In this chapter, a three-dimensional radiation simulation model for participating media is developed. This step is building toward the complex radiation exchange process inside the enclosure volume. After view factors are obtained, the radiation exchange process can be simulated using the net radiation method. First, the equation for no absorbing-emitting medium is formulated. Then, the participating medium is added into the vacuum model. All surfaces are assumed to be diffuse and gray. Diffuse signifies that absorptivity and emissivity do not depends on direction and gray indicates that emissivity and absorptivity are independent of wavelength. Therefore, the diffuse-gray assumption denotes that a surface absorbs incident radiation at a fixed fraction from all angles and wavelengths, and the emissivity and absorptivity are only functions of temperature.

3.1 Radiation heat flux

Consider an enclosure volume composed of a collection of discrete areas. Each surface has various boundary conditions imposed upon them. For example, a given surface i has a surface area A_i and temperature T_i. This surface is assumed to be small enough to be considered isothermal, which means it has a uniform temperature over the area. If the surface is too large, and the temperature diverges considerably across the area, then the surface should be divided into smaller portions so the isothermal condition is still valid. Because the surface is assumed to be diffuse and gray, the black surface results can be used to derive the radiation transfer equation. All surfaces inside the enclosure produce a complex radiation exchange process. The radiation emitted from one surface will travel through the enclosure, passing through the participating medium, and reflect after encounter another surface. The process is repeated multiple times through all surfaces, and this radiation transfer treatment is commonly known

as the net radiation method.

Radiosity (R) is defined as the total radiation heat flux leaving a surface without regard to direction or wavelength. It includes both emitted and reflected power. Irradiance (I) is the total radiation heat flux incident on the surface. From now on q_{out} and q_{inc} will be used to represent radiosity and irradiance respectly. The schematic is shown below in Fig. 3.1.

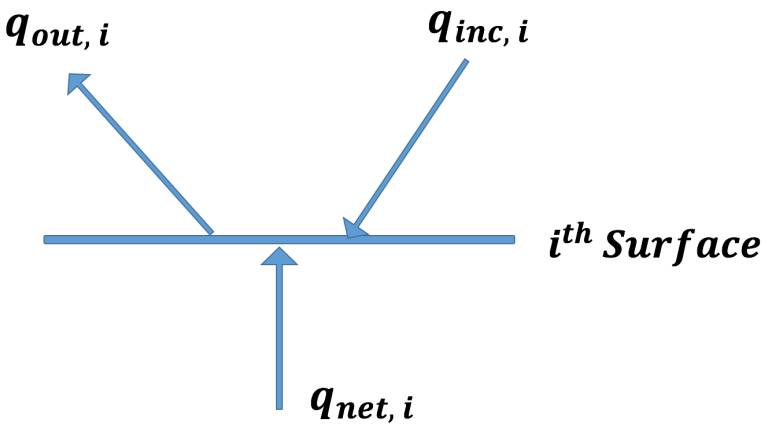

Figure 3.1: Schematic explaning the radiation heat transfer at i-th surface

The net rate of radiation heat transfer at a given surface i may be expressed as

$$q_{net,i} = \frac{Q_{net,i}}{A_i} = (q_{out,i} - q_{inc,i}) \tag{3.1}$$

where A_i is the area for surface i. From the Stefan-Boltzmann law, the rate of radiation energy emitted per unit area of the ith gray surface is proportional to the fourth power of its temperature,

$$J_i = \epsilon\, \sigma\, T_i^4 \tag{3.2}$$

where ϵ is the emissivity of the surface, and σ is the Stefan-Boltzmann constant, which is approximately equal to 5.67×10^{-8} W/m^2-K^4. Radiosity includes both the emission and reflection. For an opaque, diffuse, gray surface, the reflectivity is defined

as $\rho_i = 1 - \alpha_i = 1 - \epsilon_i$. Where ρ is the reflectivity, and α is the absorptivity. Thus, the radiosity can be written as

$$q_{out,i} = \epsilon\,\sigma\,T_i^4 + (1-\epsilon)\,q_{inc,i} \tag{3.3}$$

Similarly, the irradiance q_{inc} is defined by the total radiation heat flux incident on the surface. By using the view factor relations and summing all the incident radiation within an enclosure with N surfaces, the following expression for the irradiance is obtained

$$q_{inc,i} = \frac{1}{A_i}\sum_{j=1}^{N} F_{ji}\,A_j\,q_{out,j} \tag{3.4}$$

By substituting the view factor reciprocity relations in Eq. 2.16, the expression for irradiance can be simplified to,

$$q_{inc,i} = \sum_{j=1}^{N} F_{ij}\,q_{out,j} \tag{3.5}$$

By substituting Eq. 3.5 into Eq. 3.3, the following expression for radiosity at the *ith* surface is obtained

$$q_{out,i} = \epsilon\,\sigma\,T_i^4 + (1-\epsilon)\sum_{j=1}^{N} F_{ij}\,q_{out,j} \tag{3.6}$$

Equation 3.6 is the underlying equation for the net radiation method. A system with N surfaces will generate N different equations, which can be solved directly if sufficient conditions are provided. If the geometry is contained inside an internal enclosure, the energy will be conserved for the equation above. Additional terms need to be included in the case of an external energy source or sink on the system.

Consider an enclousure that has N surfaces, the outcome $N \times N$ system of linear equations can be formulated into a matrix. If the surface temperatures are all specified, then the q_{out} can be calculated for each surface by solving the matrix system. For example, a system of two surfaces becomes,

$$\begin{aligned} q_{out,1} - (1-\epsilon_1)F_{11}\,q_{out,1} - (1-\epsilon_1)F_{12}\,q_{out,2} &= \epsilon\,\sigma\,T_1^4 \\ q_{out,2} - (1-\epsilon_2)F_{21}\,q_{out,1} - (1-\epsilon_2)F_{22}\,q_{out,2} &= \epsilon\,\sigma\,T_2^4 \end{aligned} \tag{3.7}$$

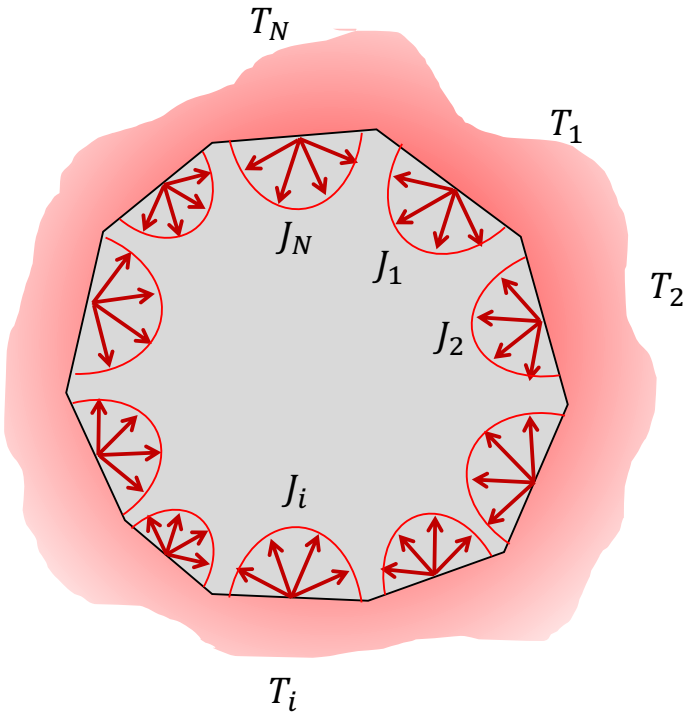

Figure 3.2: Demonstration of radiation heat transfer inside an enclosure [21]

Formulating them into matrix form, this becomes

$$\begin{bmatrix} 1-(1-\epsilon_1)\,F_{11} & -(1-\epsilon_1)\,F_{12} \\ -(1-\epsilon_2)\,F_{21} & 1-(1-\epsilon_2)\,F_{22} \end{bmatrix} \begin{bmatrix} q_{out,1} \\ q_{out,2} \end{bmatrix} = \begin{bmatrix} \epsilon\,\sigma\,T_1^4 \\ \epsilon\,\sigma\,T_2^4 \end{bmatrix} \tag{3.8}$$

Often, if the surface cannot view itself, F_{11} and F_{22} will become zero, then the diagonal terms of the matrix will be exactly 1. Since the view factors F_{ij} were calculated in advance, emissivity ϵ_i is defined as an average over the frequency spectrum. Therefore if the T_i are given through initialization, the $q_{out,i}$ can be readily solved using any numerical method. After $q_{out,i}$ is obtained, $q_{inc,i}$ can be calculated through Eq. 3.5. Then, the net radiation heat flux for a given surface can be calculated using

the difference between $q_{inc,i}$ and $q_{out,i}$.

3.2 Participating media

The equations using the net radiation method are developed by assuming that no participating medium is present inside the enclosure. More realistic, a participating medium that can absorb, emit, and scatter radiation is often present inside the porous media. When numbers of photons entering a medium, the particles and gases can affect the incoming radiation. The radiation can pass through the object remain unchanged, which is called transmission; part of it can change its direction without change of energy or frequency, which is known as scattering; and some photons can disappear with the energy transferred to the medium, which is referred as absorption. Absorption and scattering that cause the reduction in radiation intensity are together called radiation attenuation. An example of this effect is shown in the Fig. 3.3.

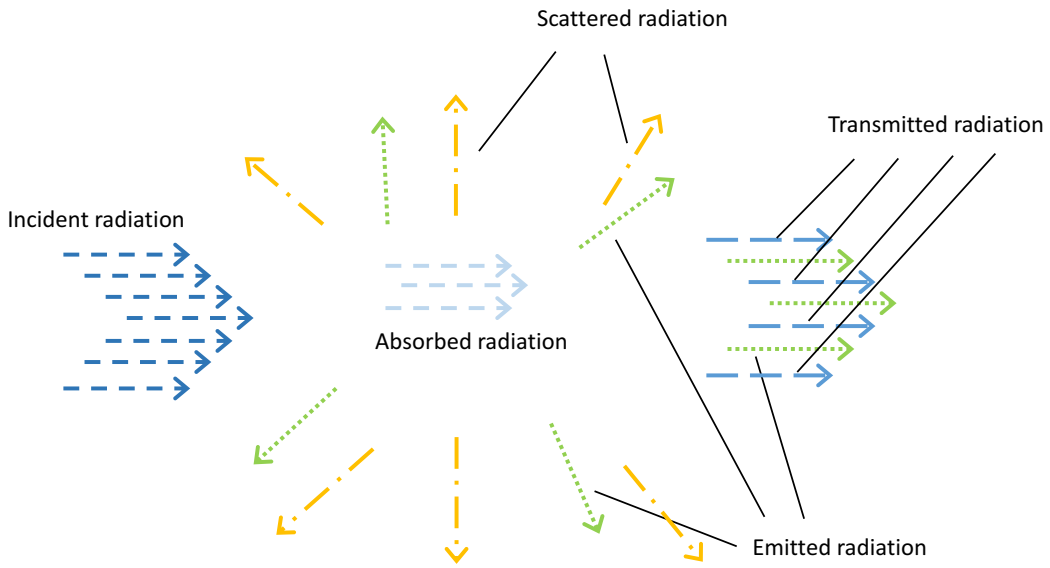

Figure 3.3: Interaction between incident radiation and participating media

These interesting but complicated phenomena have been continuously studied for over 100 years. One of the early examples is the atmosphere of the Earth interacting with solar radiation. When sunlight passes through the atmosphere, it will get attenuated by interaction with air, water, and dust. Solar radiation is scattered over the whole spectral range. Scattering is a function of the wavelength relative to the size of the particles that radiation must pass through. One of the pioneers in this area is Britain physicist Lord Rayleigh. He first described what is now referred to as Rayleigh scattering mathematically. Rayleigh scattering is an elastic process by which particles are significantly smaller than the radiation wavelength. The amount of scattering is inversely proportional to the fourth power of the radiation wavelength. This theory can also be used to explain the blue color of the sky. The blue light has a shorter wavelength than the red light, the Rayleigh scattering occurs more intensely and scatters the blue light over the sky and makes it appears to be blue.

Radiation through the gas is a common phenomenon, but the physical model is highly intricate. The difficulty for complete solutions comes from that absorption, emission, and scattering occur not only at the boundary, but at every point within the medium. Also, the gas attenuation properties often vary significantly over the spectral. Therefore, the mathematical formulations to describe the exact gas attenuation are inherently complex. Hence, the present development is only carried out at a single wavelength. Recall that the equations derived previously the surfaces are considered to be isothermal, opaque, diffuse and gray. The radiosity and irradiation from the surfaces are assumed to be uniform in all directions. Some assumptions will be made later to reduce the complexity of the equations for the participating medium.

The net radiation method developed from the previous chapter will now be extended to included the effect of a participating medium. Scattering has been neglected for the present analysis, and the total influences of the absorb-emitting medium will be refer to as gas attenuation from now on. At the ith surface of an enclosure, the

heat balance gives,

$$Q_{net,i} = q_{net,i} A_i = (q_{out,i} - q_{inc,i}) A_i \tag{3.9}$$

The radiation heat flux leaving Surface A_i is composed of the emitted and reflected energy which can be written as,

$$q_{out,i} = \epsilon_i \, \sigma \, T_i^4 + (1 - \epsilon_i) \, q_{inc,i} \tag{3.10}$$

Combine Eq. 3.9 and Eq. 3.10, $q_{inc,i}$ is eliminated and the following relation is obtained,

$$q_{net,i} = \frac{\epsilon_i}{1 - \epsilon_i} \left(\sigma \, T_i^4 - q_{out,i} \right) \tag{3.11}$$

Thus, $q_{net,i}$ can be calculated directly once $q_{out,i}$ is known. To develop the gas attenuation equations, consider the case of an enclosure with only two surfaces again, the exchange equation is given in Eq. 3.7. To account for the effect of gas attenuation, $\psi_{ij,b}$ is defined in additional to the original view factor F_{ij}. $\psi_{ij,b}$ is defined as the fraction of the energy leaving surface i that is incident with the surface j when the surface is black and the medium is in thermal equilibrium. It is a dimensionless quantity that represents the fraction of energy flux transmitted from one surface to another comparing to the black body radiation. In the radiative thermal equilibrium, no heat sources or sinks are present during the heat transfer process. The radiation absorbed at a given portion of gas must be re-emitted at that position to maintain equilibrium. Black wall relations can be extended into diffuse gray wall relations. Inside an internal enclosure, the sum of the view factor is equal to 1, which is the infinite parallel plate problem for the two surfaces case. In this case, the view factor $F_{11} = F_{22} = 0$ and $F_{12} = F_{21} = 1$ when no gas is present. For the medium case, F_{12} and F_{21} is replaced with $\psi_{12,b}$ and $\psi_{21,b}$. Since they are equal, for simplicity we will refer to them as ψ_b. Thus, $F_{11} = F_{22} = 1 - \psi_b$. Rewrite Eq. 3.7 gives,

$$\begin{aligned} q_{out,1} - (1 - \epsilon_1)(1 - \psi_b) \, q_{out,1} - (1 - \epsilon_1) \psi_b \, q_{out,2} &= \epsilon \, \sigma \, T_1^4 \quad , \\ q_{out,2} - (1 - \epsilon_2) \psi_b \, q_{out,1} - (1 - \epsilon_2)(1 - \psi_b) \, q_{out,2} &= \epsilon \, \sigma \, T_2^4 \quad . \end{aligned} \tag{3.12}$$

Solving simutaneously for $q_{out,1}$ and $q_{out,2}$ yields the following symmetry relations

$$\begin{aligned} q_{out,1} &= \frac{\epsilon_1\epsilon_2\sigma {T_1}^4 + \epsilon_1(1-\epsilon_2)\psi_b\sigma {T_1}^4 + \epsilon_2(1-\epsilon_1)\psi_b\sigma {T_2}^4}{\psi_b(\epsilon_1+\epsilon_2-2\epsilon_1\epsilon_2)+\epsilon_1\epsilon_2} \quad , \\ q_{out,2} &= \frac{\epsilon_1\epsilon_2\sigma {T_2}^4 + \epsilon_2(1-\epsilon_1)\psi_b\sigma {T_2}^4 + \epsilon_1(1-\epsilon_2)\psi_b\sigma {T_1}^4}{\psi_b(\epsilon_1+\epsilon_2-2\epsilon_1\epsilon_2)+\epsilon_1\epsilon_2} \quad . \end{aligned} \tag{3.13}$$

Substituting $q_{out,1}$ into Eq. 3.11 and rearrange

$$\frac{q_{net,1}}{\epsilon_1\sigma({T_1}^4-{T_2}^4)} = \frac{(1/\epsilon_1)\psi_b}{\psi_b(1/\epsilon_1+1/\epsilon_2-2)+1} \tag{3.14}$$

The above expression is the dimensionless heat flux ψ for the diffuse gray wall case. If both surfaces have the same emissivity this relation can further simplify into,

$$\psi = \frac{\psi_b}{2(1-\epsilon)\psi_b+\epsilon} \tag{3.15}$$

The solution of ψ_b between two infinite parallel plates in a gray gas have been obtained by many researchers. Heaslet and Warming [16] have obtained solutions accurate to four significant figures, and the value are given in the following table

The value of ψ_b can be approximated by the following function with a max error of

Table 3.1: Dimensionless heat flux ψ_b table from Heaslet and Warming [16]

Optical thickness	ψ_b	Optical thickness	ψ_b
0.1	0.9157	0.8	0.6046
0.2	0.8491	1.0	0.5532
0.3	0.7934	1.5	0.4572
0.4	0.7458	2.0	0.3900
0.5	0.7040	2.5	0.3401
0.5	0.6672	3.0	0.3016

6% at $\tau = 0$.

$$\psi_b \sim \frac{1}{1.06567+\frac{3}{4}\tau} \tag{3.16}$$

where τ is the optical thickness of the medium layer for a path of length S,

$$\tau(S) = \int_0^S \mu \, dS^\star \tag{3.17}$$

Where μ is the attenuation factor of the gas and S is the physical distance between two surfaces. Since a uniform gas absorption is assumed in the enclosure, τ can be rewritten in the linear form where $\tau = \mu\, S$. Next, this two surfaces relation is extended into the multi-surface exchange model derivated in the previous section. Implementing the heat flux ratio into the radiative transfer Eqs. 3.5 and 3.6 gives,

$$q_{out,i} - (1-\epsilon) \sum_{j=1}^{N} F_{ij}\psi\, q_{out,j} + F_{ij}(1-\psi)\, q_{out,i} = \epsilon\, \sigma\, T_i^4 \quad , \tag{3.18}$$

$$q_{inc,i} - \sum_{j=1}^{N} F_{ij}\psi\, q_{out,j} + F_{ij}(1-\psi)\, q_{out,i} = 0 \quad . \tag{3.19}$$

and for the adiabatic boundary surface, $q_{inc,i} = q_{out,i}$, equation becomes

$$q_{out,i} - \sum_{j=1}^{N} F_{ij}\psi\, q_{out,j} + F_{ij}(1-\psi)\, q_{out,i} = 0 \tag{3.20}$$

In summary, the equations are a direct extension of the net radiation method for radiation traveling through an absorbing-emitting medium. Scattering is assumed to be insignificant and the participating medium is in radiative equilibrium. No external sink or source are considered and the radiation absorbed at a given portion must be re-emitted to maintain energy balance. Note that the resulting equations for diffuse gray enclosures with participating media are only carried out in a single wavelength. It can be solved in spectral form and integrated over all wavelengths, but it involves a considerable amount of numerical work because the gas absorption properties can vary significantly with different wavelengths.

3.3 Periodic Boundary Conditions (PBC)

Often, when the geometry is not symmetrical, the heat flux at the opposite walls might not be equal. This unbalanced heat flux prevents the system from reaching steady state, and creates problems in the conductivity model. The foundation of the thermal conductivity model is based on the assumption of steady state. The

solution for the adiabatic walls is implementing periodic boundary conditions (PBC). This boundary condition is often applied to the finite size of a simulation box to compute the structure characteristic correctly. In PBC, the sample is assumed to be surrounded by an infinite number of identical systems. Therefore, the radiation leaves the enclosure at one side, an identical radiation will enter the box at the other. Note that the PBC can only be applied to the side boundaries, because the two opposite surfaces in the direction of the temperature gradient will have different temperatures. Therefore the radiation leaving the enclosure from one side can not be assumed to be equal to the radiation entering from the opposite side.

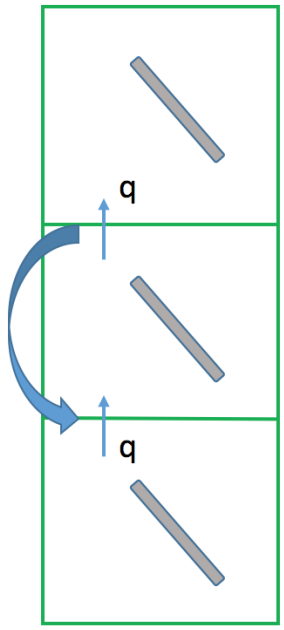

Figure 3.4: Illustration of periodic boundary conditions

To apply PBC to the matrix, a row swap is performed between two opposite surfaces. Additionally, an exchange between the diagonal term and the opposite surface at the swaping row is needed. For example, if surface 1 and 2 are the two

opposite side walls, the PBC from Surface 1 and 2 are,

$$\begin{aligned} A([1\ 2],:) &= A([2\ 1],:), \\ A(1,[1\ 2]) &= A(1,[2\ 1]), \\ A(2,[1\ 2]) &= A(2,[2\ 1]); \end{aligned} \tag{3.21}$$

Where A is the square matrix formulated by the view factor and emissivity from Eq. 3.8. Although PBC is able to solve the unbalanced heat flux from the side boundaries, the problem still remains at the surface along the temperature gradient. An iterative approach is used to resolve this problem and reach radiative equilibrium. For the asymmetry geometry, the system might not be in equilibrium with linear temperature variation along one direction. To find the radiative equilibrium temperature at each individual surface, the surface temperature inside the enclosure is iterated based on the incident heat flux as following,

$$T_i^{n+1} = \left(\frac{{q_{inc,i}}^n}{\sigma} \right)^{1/4} \tag{3.22}$$

Usually after about 20 iterations, the temperature converges, and heat flux will be balanced at the opposite surfaces. Thus, the steady state thermal energy equation based on the Rosseland approximation can be used to extract the thermal conductivity.

It is important to note that only radiation is considered during this iteration process. Therefore the steady state temperature distribution might not correspond to the actual temperature profile in reality. Radiative equilibrium requires that the radiation leaving an object is equal to the total radiation entering it. This can occur in the absence of thermodynamic equilibrium. Adding conduction during this process might correspond closer to reality and produce a more accurate result.

3.4 Conductivity model

A common approach to extract useful parameters from radiative heat transfer is using a technique similar to the conduction equation. The effective radiation heat conductivity is obtained by a systematic approach as follows. Inside the cubic internal enclosure, a small temperature difference ΔT is imposed in the n-direction between the two opposite walls ($n \in \{x, y, z\}$). The subscript $w1$ and $w2$ are used to denotes the conditions at these two walls. Meanwhile, the adiabatic condition is imposed for the other four boundary walls in the mth direction ($m \in \{x, y, z \,\&\, m \neq n\}$). The temperature gradient is only assigned in the nth direction, thus $\partial T/\partial m = 0$. Next, a constant temperature gradient is applied along the n-axis. Assuming the $w1$ has a higher temperature than $w2$, thus the ith triangle is assigned the temperature:

$$T_i = T_{w1} - \Delta T \, \frac{C_{n,i}}{L_n} \tag{3.23}$$

Here, $\Delta T = T_{w1} - T_{w2}$ is the temperature differences between two opposite walls; $C_{n,i}$ is the centroid coordinate of the triangle i in the n-th direction relative to $w1$; and L_n is the distance between wall 1 and 2. The surface emissivity is assumed to be known in advance. After the temperatures for all the surfaces are defined, Eq. 3.20 is applied for the four boundary walls and Eq. 3.18 is applied to all the remaining surfaces. A large N by N system of linear equations is formed, and the radiosity at a specific attenuation factor can be readily solved using a standard numerical method. It then follows that, the incident radiation q_{inc} can be obtained by summing all the radiosity that arrived to the ith surface using equation 3.19. Lastly, the heat flux that passed through the fiducial volume can be obtained by the net radiation emitted from Wall 1 or received by Wall 2. They will be nearly identical since the symmetry condition is imposed on the walls and the gas is in radiative equilibrium. This planar average heat flux value will be referred to as q_m for simplicity.

After q_m is obtained, the effective radiative conductivity can be determined using

a procedure based on Fourier's Law. Since the geometry is three dimensional, the heat flux written in Cartesian coordinates takes the form,

$$\vec{q}_m = q_x\,\hat{i} + q_y\,\hat{j} + q_z\,\hat{k} \tag{3.24}$$

Fourier's Law is a emperical relationship between the rate of thermal conduction in a material and the temperature gradient along the direction of heat flow, it is describes as

$$\vec{q}_m = -k\vec{\nabla}T \tag{3.25}$$

This relationship can be rewritten in the following three dimensional matrix,

$$\begin{bmatrix} q_x \\ q_y \\ q_z \end{bmatrix} = - \begin{bmatrix} k_{xx} & k_{yx} & k_{zx} \\ k_{xy} & k_{yy} & k_{zy} \\ k_{xz} & k_{yz} & k_{zz} \end{bmatrix} \begin{bmatrix} \frac{\partial T}{\partial x} \\ \frac{\partial T}{\partial y} \\ \frac{\partial T}{\partial z} \end{bmatrix} \tag{3.26}$$

where k_{mn} is the thermal conductivity tensor and $\frac{\partial T}{\partial m}$ is a temperature gradient operator with respect to x, y, z direction. For example, if the temperature difference is assigned on the x direction, then $\frac{\partial T}{\partial y} = \frac{\partial T}{\partial z} = 0$. Eq. 3.26 can be rewritten into the form,

$$\begin{aligned} q_x &= k_{xx}\,\frac{\partial T}{\partial x} \\ q_y &= k_{xy}\,\frac{\partial T}{\partial x} \\ q_z &= k_{xz}\,\frac{\partial T}{\partial x} \end{aligned} \tag{3.27}$$

Thus, the effective thermal conductivity value can be determined based on the predefined temperature gradient. For instance, if k_{xx}, k_{xy}, and k_{xz} at 300 K are of interest, a temperature difference of 1 K can be applied between two opposite boundary walls in the x-direction. One wall is assigned a temperatrue of 299.5 K, and the other wall at 300.5 K. And the surfaces between the enclosure will have a temperature ranging from 299.5 K and 300.5 K based on their centroid coordinates in the

x-direction. Using the exchange factor equations q_x, q_y, and q_z can be solved. Then k_{xx}, k_{xy}, and k_{xz} at $T = \frac{1}{2}(T_{w1} + T_{w2})$ can be readily determined. Analogous steps are applied to the thermal conductivity for the y and z axis. This process is repeated for temperatures ranging from $T \in [300, 4000]$ K. Additionally, the relationship between attenuation factor and the thermal conductivity at a fixed temperature can be investigated . Therefore the radiative conductivity value is both a function of μ and temperature T. To summarize, the exchange factor model consists of the following steps:

1. Define an internal enclosure based on the input porous structure and discretize the boundary walls into smaller grids.

2. Determine the geometry configuration factor between all the surfaces, including the boundary walls.

3. Assign $\Delta T = 1$ K in one direction between two opposite boundary walls for a specific temperature T of interest. And a linear temperature gradient is applied for all the surfaces based on their centroid coordinate.

4. Formulate the matrix based on Eqs. 3.18, 3.19, 3.20 for a specific μ, ϵ.

5. Apply re-radiating and periodic boundary conditions to the four sidewalls.

6. Solve the matrix. The net radiation heat flux is obtained by taking the difference between q_{inc} and q_{out}.

7. Iterate the surface temperature based on Eq. 3.22 until the system reaches radiative equilibrium.

8. Extract the effective radiation conductivity value by using Fourier's law from Eq. 3.25. This process is repeated along all three axes.

9. Repeat the process across different values of T, μ, ϵ to obtain a function of effective radiative conductivity k for specific samples.

It is important to note that only effective radiation conductivity is extracted from this procedure. The total effective conductivity k_{tot} of the material also includes the gas and solid conductivity, which is not discussed in this section. k_{tot} can be obtained by using the principle of superposition, and the formulation for each of the thermal conductivity terms will be discussed in more detail later with specific test geometry.

3.5 Model validation

To validate the above formulation in the radiative transfer problem, two heated, opaque walls with absorbing, emitting gray homogeneous medium in between are considered. Considerable amounts of literature have investigated this two plane radiation exchange problem. Both walls are assumed to be diffuse and gray, and the physical conditions of the walls, including the emissivity and temperature are known. The gas inside the enclosure is in radiative equilibrium with a uniform attenuation coefficient. An illustration of this problem is shown in Fig. 3.5. Since the numerical model is three-dimensional, the sidewall is specified to be very thin in order to neglect the effect of the side boundaries reflection. Therefore, instead of a cubic enclosure, the side boundaries become a rectangle with a very high aspect ratio (~ 1000); Equivalently, Distance between the two plates L is very small compared to the size of the plates. Therefore the contribution of the side boundary will be insignificant compared to the two parallel square plates. High-resolution grids are applied to the plates to ensure the accuracy of the view factor. Two parallel plates are referred to as $w1$, $w2$, and the symmetry condition is applied on side boundary walls.

The two parallel walls are assumed to have the same emissivity coefficient. Unit length L is assigned as the distance between the two square plates. In this test case, $w1$ is defined with a temperature of 300.5 K and $w2$ with 299.5 K. The radiation heat transfer between two black plates with no participating medium is described by the Stefan-Boltzmann law.

$$q = \sigma({T_{w1}}^4 - {T_{w2}}^4) \tag{3.28}$$

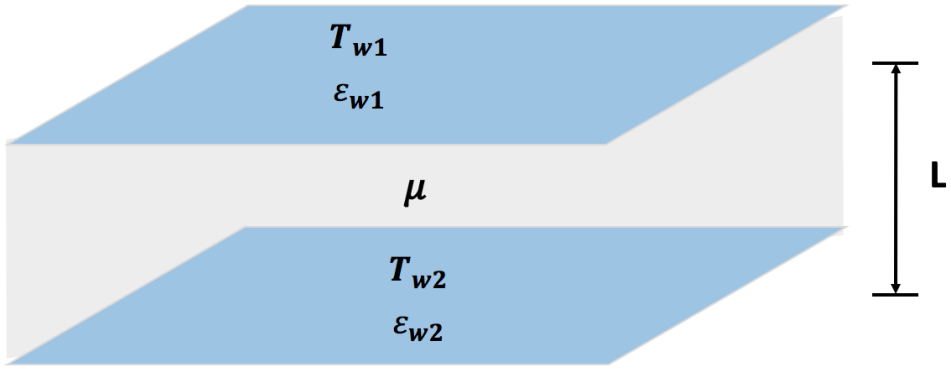

Figure 3.5: Illustration of two parallel walls test case subject to participating medium.

where σ is the Stefan-Boltzmann constant. When the surface is black, the absorptivity becomes unity, there will be no reflection and the radiosity is only composed of the emitted energy. This equation gives the maximum rate of radiation exchange between two surfaces. The procedure for obtaining the heat flux using the exchange factor model was discussed in the previous section.

Figure 3.6 plotted the q_{inc} and q_{out} for the two parallel plates using the exchange factor model when $\epsilon = 0.8$. The radiosity and irradiance showed a symmetry behavior between two plates. As optical thickness increases, the incident radiation from $w2$ decreases, while the incident radiation from $w1$ increases at the same rate.

The radiation heat flux between two parallel plates can be obtained by taking the difference between $q_{inc,w1}$ and $q_{inc,w2}$. It is important to highlight that the net heat flux emitted from $w1$ is expected to be virtually identical to the net heat flux received by $w2$. The analytical results used for comparison were obtained from the diffusion solution by Robert Siegel and John Howell in the Thermal radiation heat transfer book [40]. The result is plotted in Fig. 3.7

The black line represents the analytical solution and the red dot is the numerical

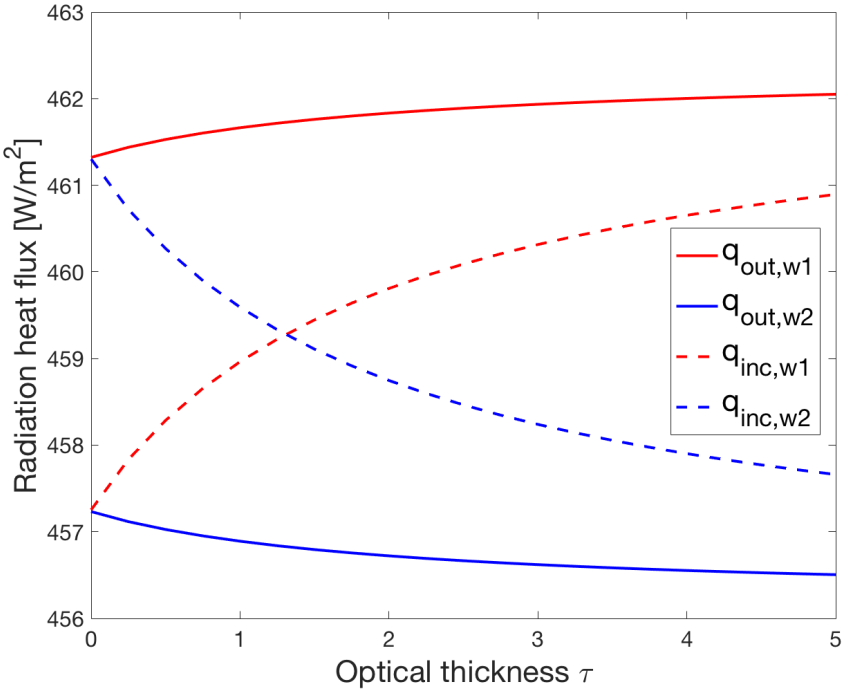

Figure 3.6: Variation of radiation heat flux with optical thickness for absorbing, emitting medium at various emissivity coefficient (Two infinite parallel wall test case).

result from the exchange factor model developed in this research. An excellent agreement is observed with this proposed model and the analytical solution. When the medium is transparent ($\tau = 0$), and the surfaces are black ($\epsilon = 1$), the radiation heat flux is expected to be identical with the q from Eq. 3.28. As the optical thickness increases, the radiation heat flux is decaying due to gas absorption. Radiation heat flux also decreases as the emissivity value decreases. Note that as the emissivity comes closer to 0, the radiation heat flux becomes independent of the optical thickness, since less ratio of thermal radiation will be emitted from the surface.

3.6 Wedge geometry

A simple wedge geometry was created to investigate the behavior of the iterative approach and validate the performance of the model for three dimensional cases.

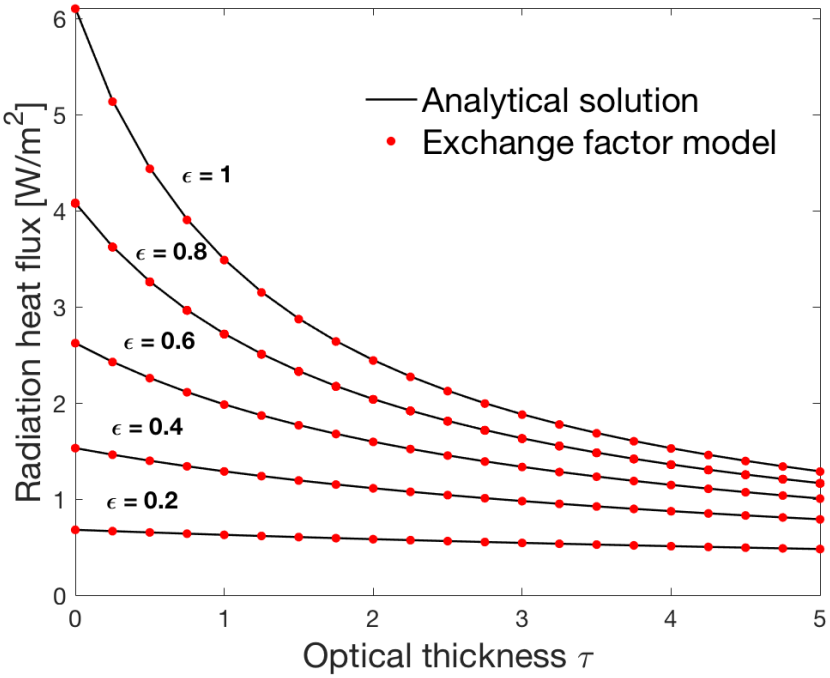

Figure 3.7: Variation of radiation heat flux with optical thickness for absorbing, emitting medium at various emissivity coefficient (Two infinite parallel wall test case).

It was noted that the heat flux at the opposite walls might not be balanced if the geometry is asymmetric. For this right triangular prism, the x and y directions are dissymmetry, while the z direction is symmetry. The wedge is created by 2 right triangles and 3 rectangular sides. Since the triangle is isosceles, the bottom and left sides are actually squares.

A surface discretization was performed to decompose the geometry into fine triangular meshes. Additionally, an enclosure box was created to contain the wedge inside. Since this geometry is relative simple, a highly refined mesh was used to ensure accuracy. A constant value of emissivity $\epsilon = 0.85$ is used and no participating medium is accounted for. After implementing the model without iteration, the heat flux values was plotted in Fig. 3.9.

From Fig. 3.9, the normalized heat flux along the temperature gradient direction is plotted against the unit distance. A $\Delta T = 0.1$ K is applied along x, y, and

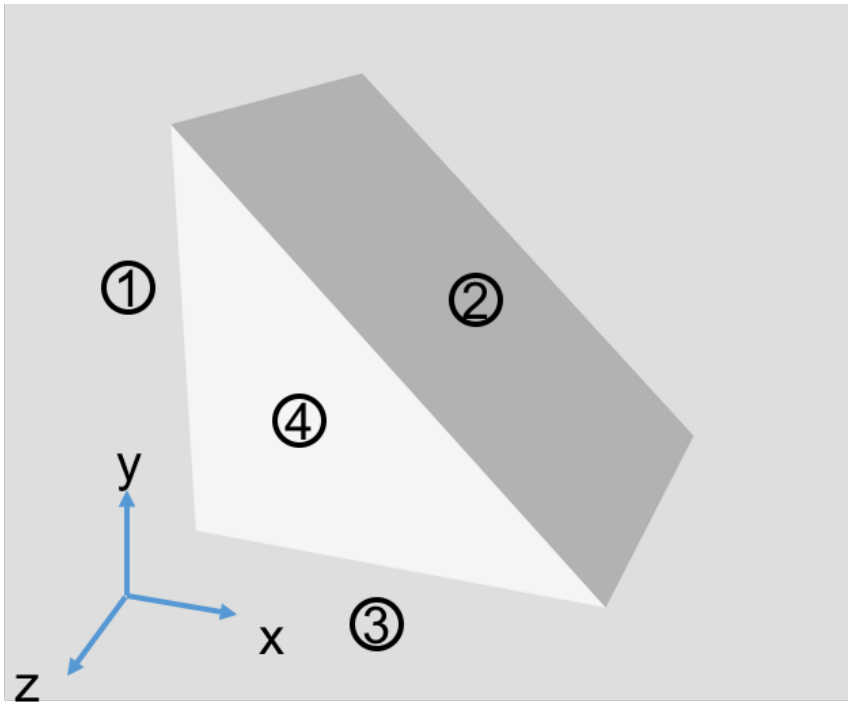

Figure 3.8: Isosceles right angled triangular prism used for the three dimensional verification test case

z directions; the heat flux values are represnted by red, green, and blue markers respectively. The heat flux at boundary walls is located at unit ditance equal to 0 and 1. In the direction of symmetry (z direction), the heat flux across the wedge is symmetric about the midpoint, and the heat flux at the wall is identical. However, for the asymmetry directions (y and z direction), the heat flux along the distance is unbalance and the opposite wall heat flux is not equal. Assuming the temperature gradient is applied in the x direction, although the total view factor from the left wall to surface 1 is higher than the total view factor from the right wall to surface 2, but the temperature difference is in contrast. These two effects do not cancel out and result in unbalanced heat flux.

The heat flux distribution showed that the geometry is not in steady state with the linear temperature gradient, thus iteration on the surface temperature is performed until the system reaches radiative equilibrium. By using Eq. 3.22, the heat flux at the

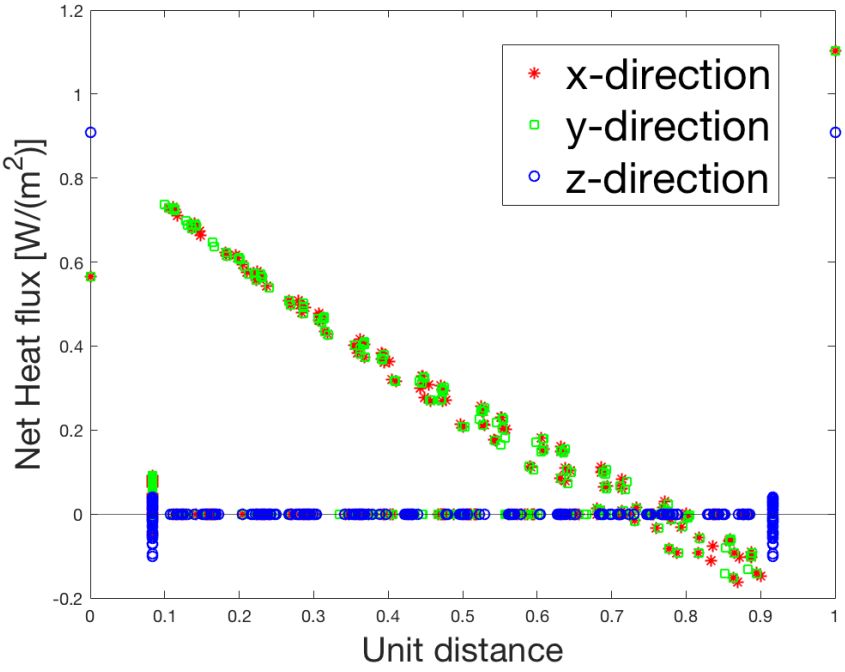

Figure 3.9: Normalized heat flux at 500K for the prism geometry, $\Delta T = 0.1K$

opposite walls converged to the same value in about 10 iterations. Note that the q_{net} from the plot is absolute values because one side has a negative net heat flux since the radiation is leaving the surface.

After the system reached steady state, the temperature distribution no longer has a linear variation along the principle direction. For example, if the temperature gradient is applied in the x direction initially, the temperature distribution at surface 1 and 2 after the system reaches equilibrium will be most interested. The teperature profile is plotted below in figure 3.11, 3.12.

A clear and uniform pattern is shown in Figs. 3.11 and 3.12. For Surface 1, the equilibrium temperature is the highest at the center and decrease as it moving outward. For Surface 2, the temperature decreases as along the x'-direction, which is the length of the inclined rectangular surface. Discontinuity is observed between the surfaces since only radiation is considered, no conduction is present inside the solid.

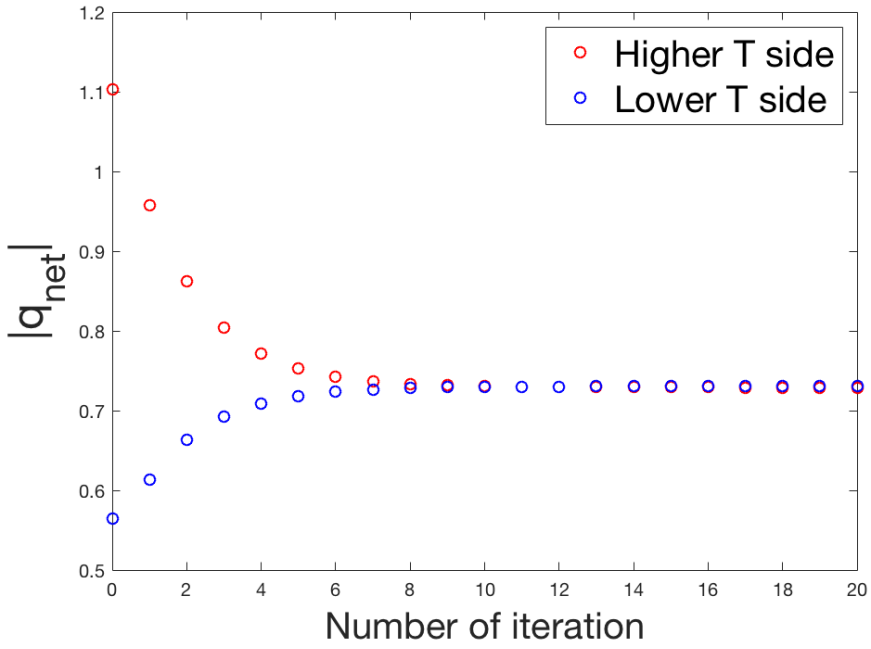

Figure 3.10: Heat flux at the opposite wall with x direction temperature gradient for prism test case.

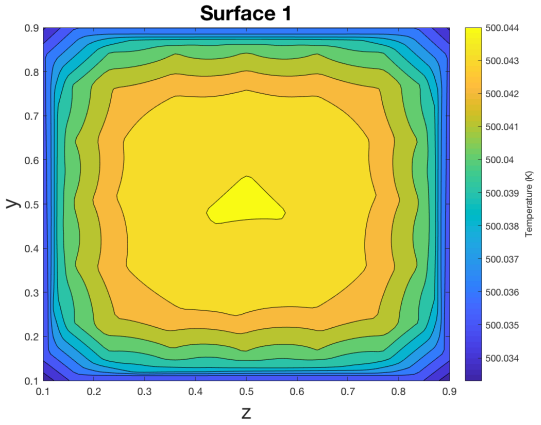

Figure 3.11: Steady state temperature profile at surface 1 for the prism test case

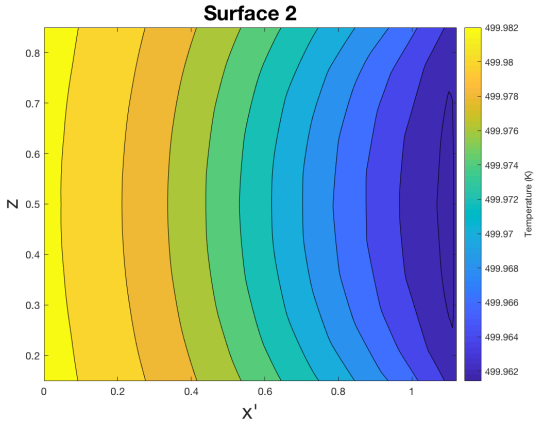

Figure 3.12: Steady state temperature profile at surface 2 for the prism test case

For this wedge geometry, the conduction would play a critical role for the temperature distribution, and would produce different heat flux values at the boundary walls. However, coupling radiation with conduction is not the focus of this research. With the porous material, internal conduction will be less relavent since only small

percentage of the volume are composed of actual fibers. Additionally, when the temperature is extremely high like during atmospheric entry, the radiation will dominate conduction, and become the primary mode of heat transfer.

Chapter 4 Results

4.1 FiberForm real geometry

Background

To prepare for the future mission of space exploration and meet the requirement of thermal protection system (TPS) in a more demanding atmospheric entry environment. NASA has been investing in better performance and more effective heat shield material called Phenolic Impregnated Carbon Ablators (PICA). PICA is an ablative material that carries the heat away mostly by convection and radiation. This lightweight and reliable heat shield has been used frequently on modern spacecraft. Its performance has been validated by the success of the MSL and Mars 2020 missions. To gain a better understand of the performance of PICA at the microscopic scale, NASA conducted X-ray experiments to construct the microscale structure and track the material's response to extreme temperatures and pressures [23]. The thermal protection system can be improved and optimized with a deeper understanding of the preform architecture and properties. Here, the radiation exchange model is implemented into a small sample of FiberForm shown in figure 4.1. This sample was generated by Lawrence Berkeley National Laboratory (LBNL) using Advanced Light Source. The X-ray sample has been studied by Nouri et al. [33] previously, where the effective radiation conductivity for FiberForm without participating medium was investigated. This research extends his analysis accounting for the participating medium with the new proposed radiation exchange model.

The carbon substrate in PICA is called FiberForm. Radiation is a critical mode of heat transfer during atmospheric entry since heat flux is extremely high and FiberForm has a porosity of approximately 88%. Studying the radiation exchange process of FiberForm at a microscale level could provide useful information to improve the per-

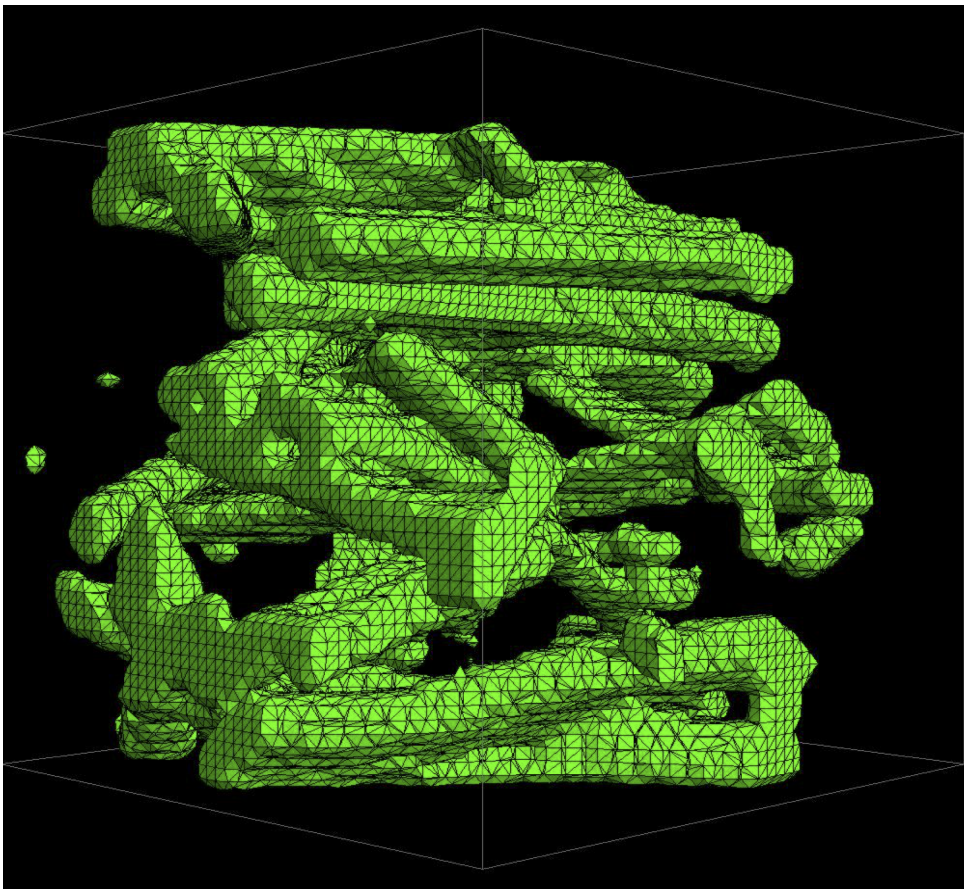

Figure 4.1: 3D microscopic scale sample of FiberForm real geometry extracted from computed tomography [31].

formance, and help understand how the porous structure and participating medium impact the material properties.

The microscale sample is composed of triangular surface elements to characterize the microstructure of the real FiberForm sample. The average diameter of the fiber is about 10.6 μm and the size of the sample is $0.1 \times 0.1 \times 0.1$ mm^3. The geometry data is in STL format and it contains 56,268 triangle surfaces in total. The vertices coordinates were given from the data file and centroid locations for each triangle surface can be calculated by taking the average from each vertex in different directions (i.e. $C_x = \frac{1}{3}(V_{1,x} + V_{2,x} + V_{3,x})$). The cubic boundary walls are defined in a way that all the triangular surfaces are contained inside the internal enclosure. A mesh

that divided the boundary wall into subsection that is approximately equal to the size of the triangle is used in here. Higher resolution can be used if desired, but more computational cost will be required. All surface elements are assumed to be diffuse, gray, and isothermal. The boundary walls are considered to have the same properties as the surface elements. The absorbing-emitting medium that filled the pores is assumed to be in radiative equilibrium, and the gas properties are considered to be independent of wavelength. The internal enclosures are assumed to be perfectly insulated such that there will be no external heat gain or loss.

FiberForm results and discussion

For the one-dimensional energy transfer problem without work and natural convection, the governing energy equation from Eq. 1.3 can be reduced to the following form,

$$\rho\, c_p \frac{\partial T}{\partial t} = \frac{\partial}{\partial y}(k_c \frac{\partial T}{\partial y} + q_r) \tag{4.1}$$

This equation describes the combined radiation and conduction problem with participating medium. Where k_c includes conductivity from both solid and gas conduction, and radiant heat flux q_r can be expressed by the Rosseland approximation. By grouping the radiation and conduction terms by defining effective thermal conductivity, Eq. 4.1 is reduced into

$$\rho\, c_p \frac{\partial T}{\partial t} = \frac{\partial}{\partial y}\,(k_{eff} \frac{\partial T}{\partial y}) \tag{4.2}$$

with the total effective thermal conductivity k_{eff} equal to

$$k_{eff} = k_{sol} + k_{gas} + k_{rad} \tag{4.3}$$

where k_{eff} represents the ability of a material to transfer heat through the porous body; k_{sol} is the conductivity through the solid structure or between fibers; k_{gas} is the conductivity for the fluid filling the voids between the solids, and k_{rad} is the radiation conductivity driven by the temperature gradient across the insulation. Note that k_{sol} and k_{gas} do not indicate the true conductivities of the solid and gas, they represent the

contribution of solid and void conduction in the overall heat transfer process inside the porous media.

The radiation conductivity is obtained by a systematic procedure described previously. The value of the radiative thermal conductivity calculated using the present method from 300-4000K without a participating medium is plotted in Fig. 4.2. A uniform value of 0.85 for emissivity is used here. Although emissivity often depends on temperature and wavelength, it was demonstrated by Codron et al. [6] that the emissivity of FiberForm remains nearly constant around 0.85 at different temperatures and wavelengths.

A boundary wall distance study was performed to ensure the independence of the results. Ideally, the shorter the distance would better represent the true microscale structure of FiberForm, but additional complication occurs on the calculation of view factors which cause the model to fail. Distances of 0.4% and 1% relative to the sample length were applied between the boundary wall and the FiberForm geometry, and only minor differences are observed. Therefore the boundary distance is assumed to be close enough to represent the actual radiation transfer process within the enclosure. However, the model fails when the distance is 0.1% or less. There are two possible causes for this failure. The differential view factor equation fails to represent the actual view factors when the distance between two surfaces is too close compared to the surface area. This is due to the limitation of the view factor differential approximation equation. Another possible reason is when the boundary wall is too close. Blockage filter might lead to some surface being considered totally blocked while only being partially blocked. This brings challenges to the bounding properties of the model, and poses problems to the numerical results.

From Fig. 4.2, the blue, red, and yellow lines represent the thermal conductivity in x, y, z directions respectively. They are clearly higher than off-diagonal terms plotted by the green dashed lines. The off-diagonal terms are about one order of magnitude lower than the diagonal terms. From the Rosseland radiation approximation, k_{rad} is

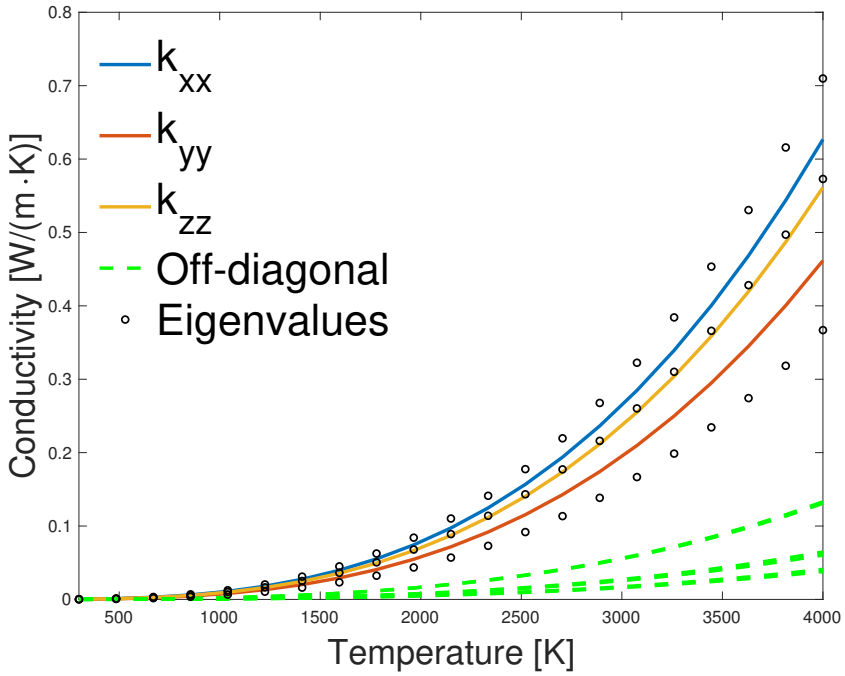

Figure 4.2: Effective radiative conductivity matrix as function of temperature without participating medium for the real FiberForm geometry($\mu = 0$).

expected to have a third-order dependency on temperature. Therefore, the geometric factor K_{mn} can be extracted by fitting a cubic polynomial of temperature,

$$k_{mn} = K_{mn}\epsilon\sigma T^3 \tag{4.4}$$

From matrix theory, eigenvalues of K_{mn} represent the effective radiative conductivity tensor when the geometry is oriented in a way that off-diagonal terms are zero. The K_{mn} matrix and its associated eigenvalues Λ is presented in Table 4.1.

From the orthotropic behavior of the conductivity matrix, FiberForm is expected to have an in-plane (IP) and through-the-thickness (TTT) direction. The eigenvalues are also plotted in Fig. 4.2 by the black dots. From the plot, one eigenvalue appears to be lower than the other two, which is the TTT direction. The TTT direction κ_{ii} is defined as $\kappa_{ii} \ll \kappa_{jj}, \kappa_{kk}$, where κ_{jj}, κ_{kk} are the IP direction. The two IP conductivity are represented by x and z direction in this case.

Table 4.1: Geometric factor reconstructed from Rosseland model and its associate eigenvalues

$K\,[10^{-4}\text{ m}]$			
	x	y	z
x	2.032	0.209	0.133
y	0.196	1.496	0.431
z	0.123	0.424	1.820

$\Lambda\,[10^{-4}\text{ m}]$			
	1	2	3
	2.301	1.857	1.189

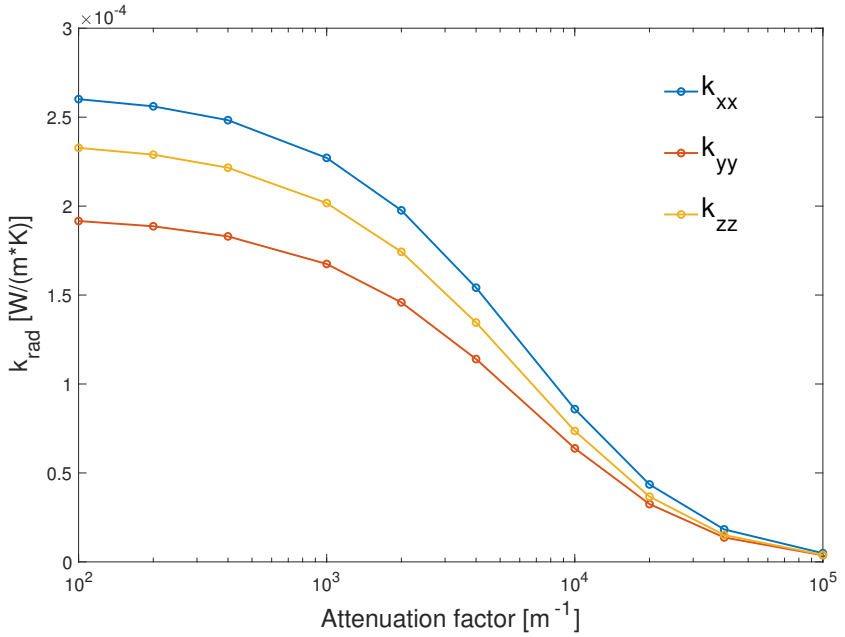

Figure 4.3: Numerical prediction for diagonal effective conductivity as function of attenuation factor for real FiberForm($T = 300K$).

The effect of participating medium is plotted in Fig. 4.3. The mean temperature was set at 300K and a constant value of 0.85 is used for the emissivity. The diagonal radiation conductivity decrease asymptotically as the attenuation factor increases.

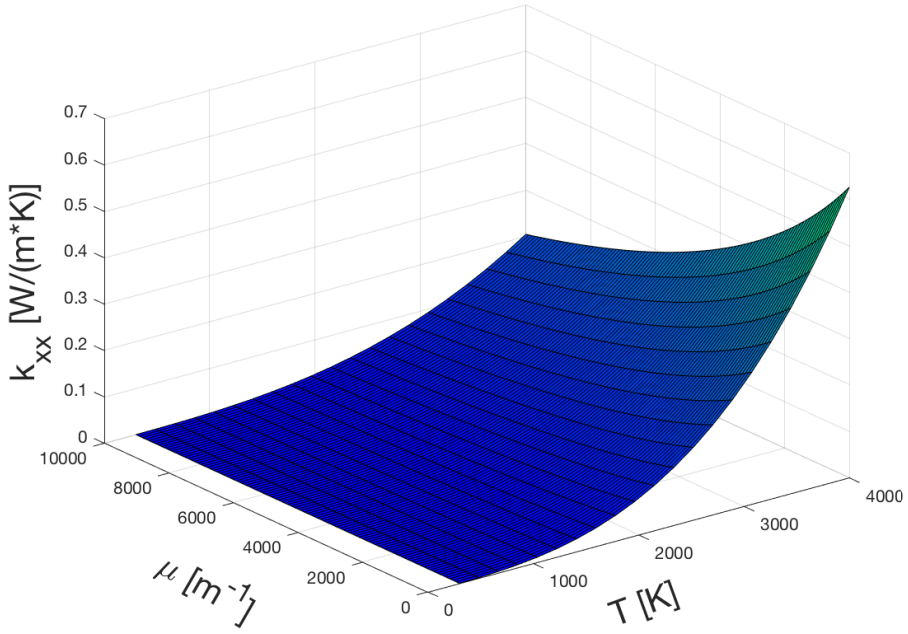

Figure 4.4: Surface plot for the temperature and attenuation factor on effective conductivity for real FiberForm k_{xx}.

The conductivity values can be appoximate by a rational functions as shown in Eq. 4.5

$$k_{xx}(T,\mu) = 2.0319 \times 10^{-4} \epsilon \sigma T^3 \left(\frac{2.164 \times 10^8}{\mu^2 + 3.471 \times 10^4 \mu + 2.164 \times 10^8} \right) \tag{4.5}$$

Eq. 4.5 is presented as a surface plot in Fig. 4.4. The conductivity value is represented by both the height and color. When the attenuation factor is 0, the terms in the parentheses will become 1 and the same Geometric factor predicted by the Rosseland approximation is obtained. This equation is able to predict the conductivity for this particular FiberForm sample at specific temperature and emissivity value. Note that the third order temperature dependency is still valid with the participating medium, which agrees with the theory from Rosseland.

4.2 Artificial geometry

Besides the real FiberForm microscale sample, artificial FiberForm is used to study and compare the numerical results. Artificial samples were created to reconstruct the micro struture of FiberForm using OTTER [28]. OTTER is a structure generation toolkit that can generate microscale fibers with desired porosity. Artificial sample is able to mimic the appearance, but the actual thermal and metchanical properties still remain unknown. A statiscal analysis was performed using the FiberForm sample cuts. For these artificial samples, the average porosity is about 88%. The length of these cubic samples is about 165 μm and the diameter of the fiber is 11 μm.

Figure 4.5 shows the five FiberForm samples generated by OTTER, each is a small section of a larger structure. Although it is not obvious visually, these three-dimensional random fibrous geometries are expected to have in-plane (IP) and through-the-thickness (TTT) direction. For the IP direction, the fibers are randomly oriented and they are anticipate to produce similar properties in both IP axis. For the TTT direction, the cylinders are generated one at the time and dropped into the box from above with approximately 15° from the pressing plane. The TTT direction is expected to have different thermal and mechanical properties than the IP direction. However, since the five samples are only a portion of a $1 \times 1 \times 1$ mm^3 sample, it reamins unknown if that is still the case at this scale level. To investigate if this morphological characteristic would be captured from the microscale radiative exchange model, multiple samples were created to compared the principal axis radiation conductivity.

From the artificial samples, the boundary distance is defined as 1% of the sample length. A uniform value of 0.85 for emissivity is used again, and the attenuation factor is set to 0 for the statistical analysis. The initial average temperature is 500 K with the $\Delta T = 0.1$ K. Linear variation in temperature along one direction is assigned to all the surfaces corresponding to their centroid coordinate. Since all the samples are three dimensional and asymmetric, an iterative approach is implemented to obtain balanced heat flux along temperature gradient direction. Figure 4.6 plotted the heat

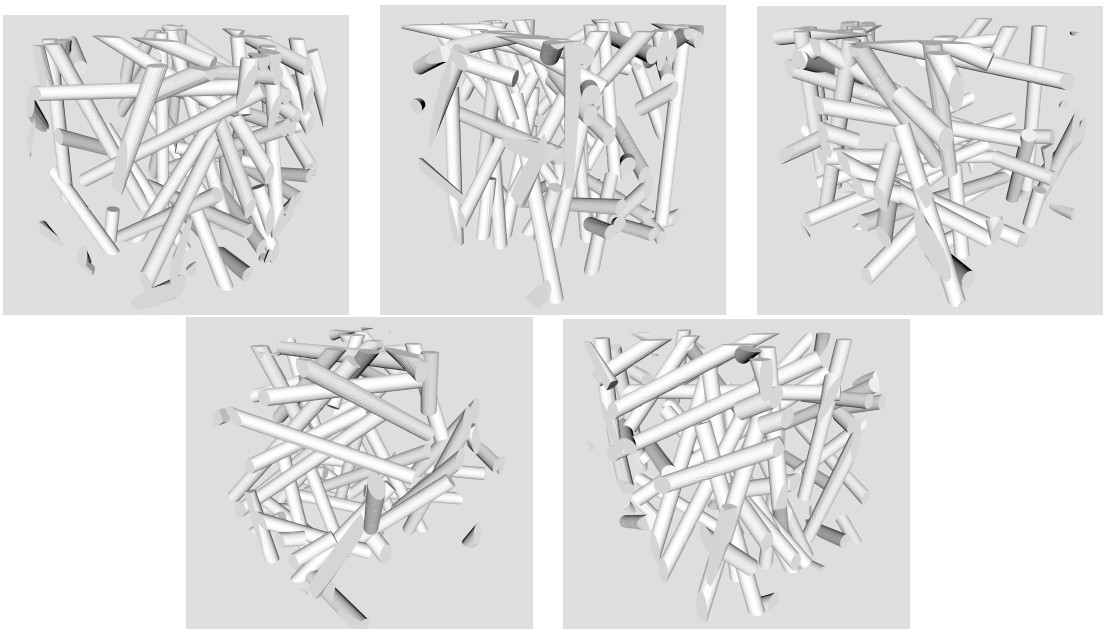

Figure 4.5: Five different artificial FiberForm sample cuts created by OTTER.

flux at the opposite wall along principle axis versus number of iterations for the first sample. Initially, the heat flux at the opposite wall is not equal, and the unbalance heat flux prevents the system from reaching equilibrium. In about 20 iterations, the $|q_{net}|$ converges to the same value for all three directions. Note that due to the numerical error of view factors calculation, it is possible to have small differences between the opposite wall heat flux after reaching steady state. Thus, the average between the q_{net} at the two opposite walls is used as the value of radiation heat flux.

With the steady state heat flux, Fourier's law can be used to extract the thermal conductivity. Equation 4.4 is applied to obtain the K_{mm}. K_{mm} is a temperature independent geometric factor associated with radiative conductivity. It is convenient to define K_{mm} since the radiative conductivity was demonstrated to have a third order temperature dependency. Thus, only one temperature needed to be evaluated to obtain the relationship between radiative conductivity and temperature. To compared K_{mm} along the principal axis, all 5 artificial samples were run to investigate the directional dependency of the thermal properties.

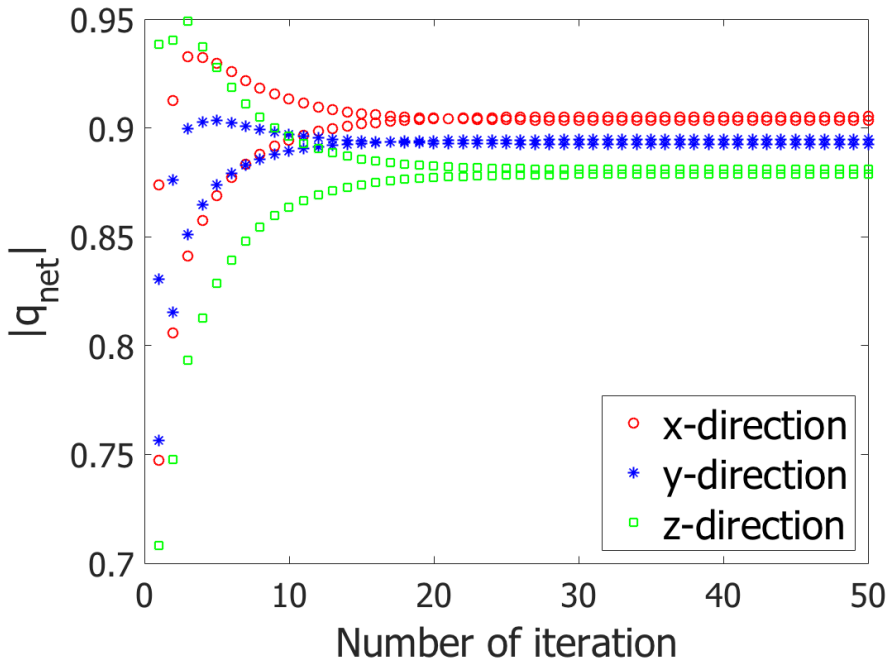

Figure 4.6: Convergence of the heat flux at opposite walls from artificial sample #1 (Fig. 4.5 top left).

Figure 4.7 illustrates the principle axis thermal conductivity for five artificial sample cuts. Besides sample #4, no obvious directional difference in radiative conductivity is shown. The z direction appears to be more uniform around the mean value but sample quantity is too small to draw a conclusion. A normal distribution plot is shown in Fig. 4.8. Although no significant difference is seen between mean values, the z direction conductivity seems to have a different shape when compaing to the conductivity from x and y direction.

From each individual sample, it is difficult to conclude the transverse isotropic behavior of the artificial FiberForm since each sample is only a small part of a larger structure. A larger sample quantity is needed to performed the statistical analysis and draw conclusions. Thus, more samples were generated and evaluated through statistical approach to obtain the actual radiative properties distribution of FiberForm.

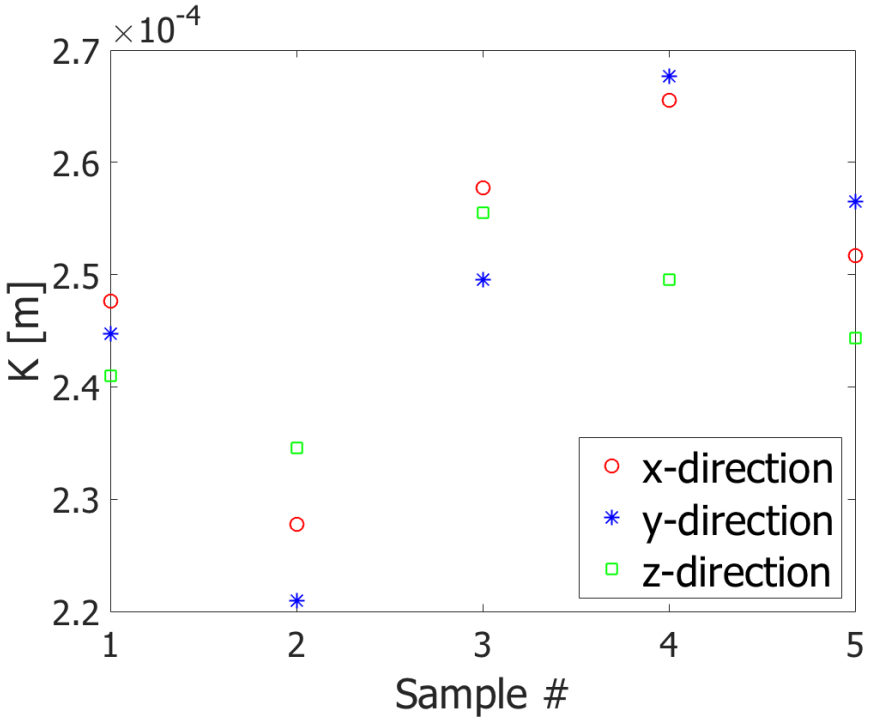

Figure 4.7: Principal direction radiative conductivity for five artificial FiberForm samples corresponding to Fig. 4.5.

Fibergen samples

Since more samples were needed for the statistical analysis, 30 more artificial FiberForm samples were generated using a different algorithm called FiberGen. FiberGen is a structure generation code that can create the desirable microstructure of fibrous material by defining fiber length, diameter, orientation, and bulk porosity, etc. More details about FiberGen can be found in the article from Stern et al. [42]. In these 30 artificial samples, the average porosity is about 87%. The length of these cubic samples is about 165 μm and the nominal diameter of the fiber is 11 μm. Each sample is generated independently instead of a small portion cut from a larger structure. Again, the fiber is expected to have IP and TTT directions. From Fig. 4.9, it is clear that the fiber has a anisotropic behavior from simple visual inspection.

The same surface properties and temperature conditions are used for these 30

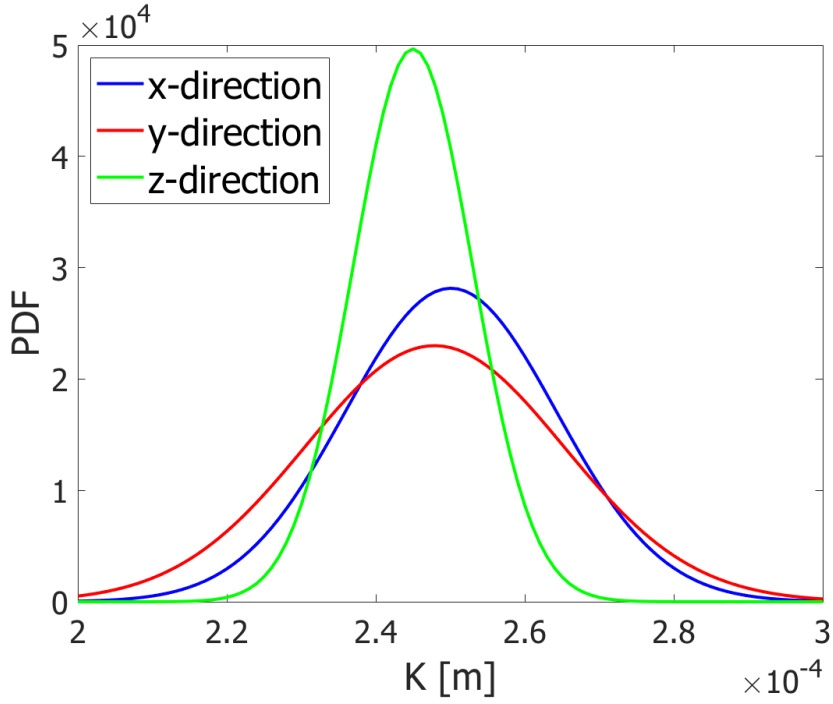

Figure 4.8: Probability distribution function along principal directions for five FiberForm samples created by OTTER.

FiberGen samples. An iteration loop was implemented to achieve steady state. To obtain the temperature distribution after reaching radiative equilibrium, the sample is divided into 300 slices along the temperatrue gradient direction, and the average temperature is taken for all the surface in each slice region. The temperature distribution after equilibrium is plotted in Fig. 4.10. The initial and equilibrium temperature are represented by red and blue lines respectively. The green lines represent the temperature within one standard deviation. The initial temperature linearly varies from 500.05 K and 499.95 K; the equilibrium temperature is mostly monotonic with the temperature decreasing as the unit distance increases.

To ensure that the temperature does not vary along any other direction, the middle slice surface temperature is plotted against the y and z direction. From Figs. 4.11 4.12, the red line is the least squares regression fit for the temperature data. No apparent temeprature gradient was observed along y and z axis when temperature

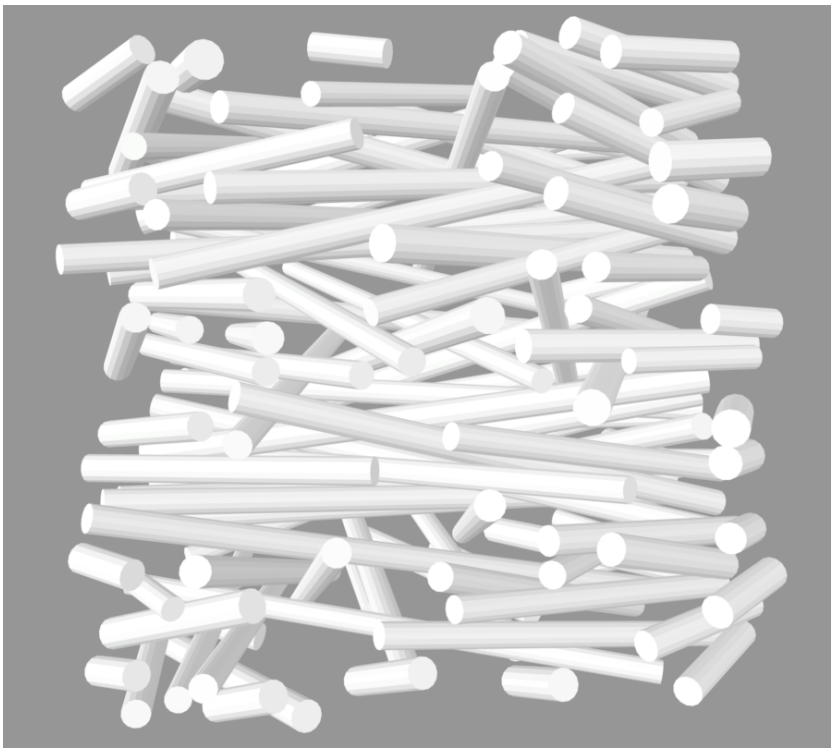

Figure 4.9: Illustration for one of the artificial FiberForm sample created by FiberGen.

difference is applied in x direction. Thus, Fourier's law from Eq. 3.27 can be used to extract the thermal conductivity value.

A conductivity distribution plot for a total of 30 artificial FiberForm samples was created in Fig. 4.13. A bell shape is observed with the highest point near the mean value. The conductivity distribution is roughly symmetric and unimodal with no outliers. Thus, a normal distribution can be used to represent the radiative conductivity value. The mean value for the radiative conductivity is 0.9225 W/m-K with a standard deviation of 0.0627 W/m-K.

Effective conductivity elements as a function of temperature for one FiberGen sample is also plotted in Fig. 4.14. The k_{xx} and k_{yy} represented by blue and red line are almost overlapping in the figure, while the z direction has a noticeably lower conductivity value. As demonstrated earlier, the diagonal conductivity is significantly higher than the off-diagonal conductivity. Since the third order temperature depen-

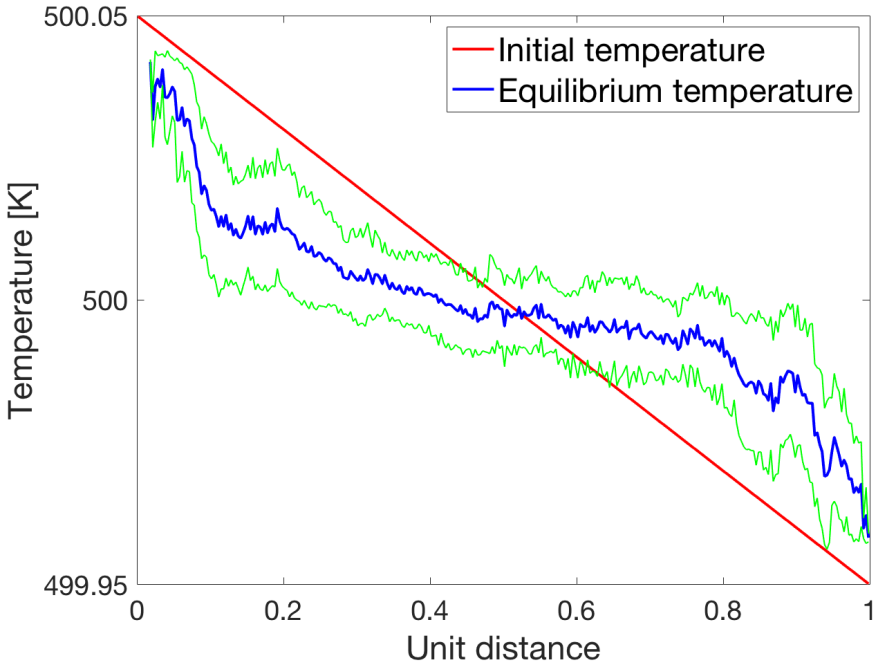

Figure 4.10: Temperature distribution along the initial temperature gradient direction for FiberGen sample at equilibrium.

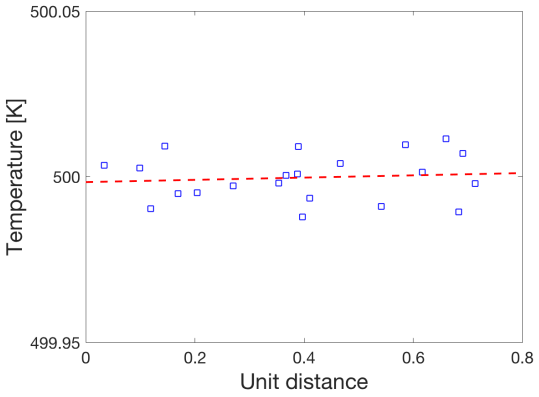

Figure 4.11: Centerline temperature along y direction, red dashed line is the least squares regression fit.

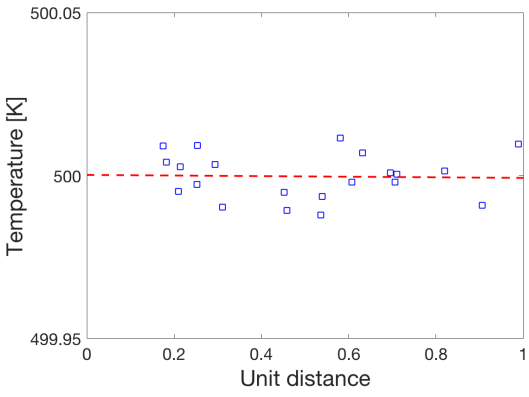

Figure 4.12: Centerline temperature along z direction, red dashed line is the least squares regression fit.

dency from the Rosseland approximation has been confirmed, only one temperature is needed to evaluate the conductivity as a function of temperature. For instance, if the conductivity matrix is extracted at 500 K, the geometric factor K_{mn} can be

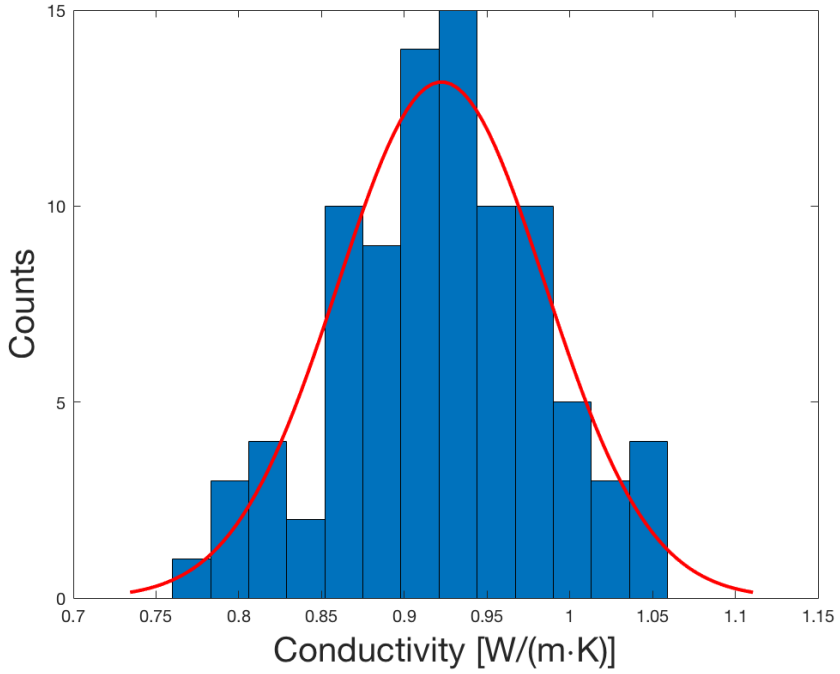

Figure 4.13: Conductivity distribution plot along principal directions for 30 artificial FiberForm samples created by FiberGen.

determined and the conductivity at different temperatures can be obtained using Eq. 4.4.

To confirm the anisotropic behavior of FiberForm, a probability density function was generated with normal distribution along all three principal axis. From Fig. 4.15, the blue, red, and green represent the conductivity distribution along x, y, and z direction respectively. The p value for these 3 lines against the null hypothesis that the data has a standard normal distribution is 0.4642, 0.7262, and 0.9552 respectively. Thus, the test failed to reject the null hypothesis with a 5% significance level, and the conductivity values can continue to be represented by a normal distribution. It is clear that the z direction is the IP direction, which has a lower thermal conductivity value than x and y direction. The mean value for K in the z direction is 2.445×10^{-4}m, while mean K for x and y direction are 2.577×10^{-4}m and 2.558×10^{-4}m respectively. Thus, transverse isotropic property is highlighted among the three dimensional artificial

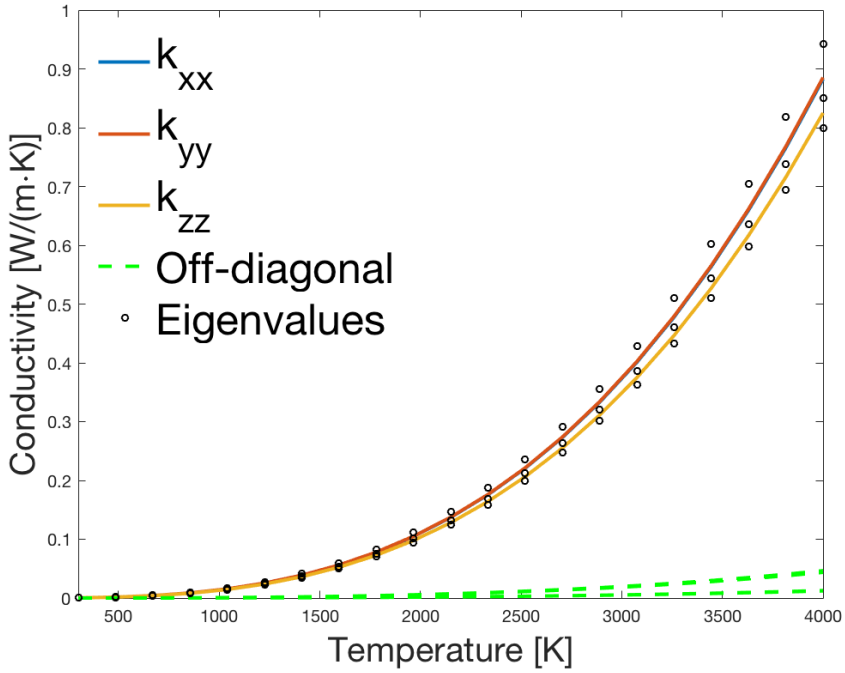

Figure 4.14: Effective conductivity matrix elements as a function of temperature for FiberGen sample.

FiberForm samples created by FiberGen.

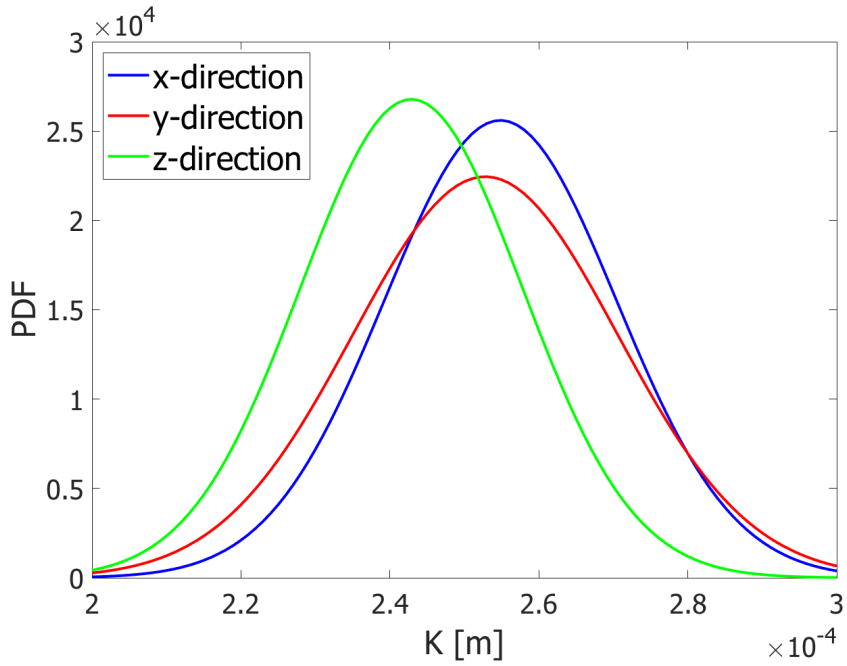

Figure 4.15: Principal axis K distribution plot from 30 artificial FiberForm samples created by FiberGen.

Chapter 5 Summary and conclusions

5.1 Summary

Experimentally measuring the radiation heat transfer through porous media is a difficult task since it is challenging to differentiate the contribution of conduction and radiation. Experiment equipment is usually expensive and it only works for limited conditions. Additionally, the effect of optical thickness is hard to obtain experimentally especially at high temperature. To overcome these difficulties, an inovative method was proposed based on the microscale structure of the fibrous material.

This research aims to develop a numerical model to evaluate the radiative conductivity based on the microscale structure of fibrous material. More specifically, on a carbon-based fibrous material called FiberForm used as a heat insulation material in TPS. In addition, the model quantitatively investigated the impact of surface emissivity and gas attenuation factor on effective radiative conductivity. The model is a direct extension of the exchange factor method, which requires the raw geometry data file that is represented by small triangle surface elements. After calculated the view factor between all the surface elements, the diffuse-gray radiative transfer equations within the enclosure can be formulated, and the effective radiative conductivity can be extracted based on the Rosseland approximation.

The absorbing-emitting medium that filled pores is treated as an extension to the two surface relations. The radiation attenuation due to gas absorption produces a rational decay relation as the optical thickness increases. By imposing a temperature gradient and collecting the net heat flux at the boundaries, radiative conductivity can be extracted using Fourier's law. The off-diagonal conductivity is obtained by adiabatic wall assumptions and periodic boundary conditions. In the case of asymmetric geometry, an iterative approach was used on surface temperature to achieve

radiative equilibrium. It was once again demonstrated that the diagonal thermal conductivity is significantly larger than off-diagonal ones. The radiative conductivity is expressed by a function over a wide range of temperature and gas attenuation factors. The nine elements of conductivity tensor showed cubic dependence on temperature as predicted by Rosseland's model. The stastical analysis from the artificial FiberForm sample highlighted the tranverse isotropic behavior of the fibrous material. Where one side has a lower conductivity value than the other two.

In conclusion, the possibility of using X-ray micro-tomography or artificial microscale structure to calculate radiative conductivity was demonstrated. An algorithm was developed which accounts for the participating medium during the radiation transfer process within fibrous material. The code has been integrated with the message passing interface (MPI) to allow parallel processing to accelerate the computational process. This numerical model has been demonstrated to be robust and accurate from the verification case. Conclusively this research aims to increase the understanding of radiation through porous media, and the modeling of radiation exchange process in fibrous material provides foundation to create more efficient and reliable thermal protection in the future.

5.2 Future studies

1. **More complex geometry**

   Even though the model can deal with complex geometry, the computational time cost would rise accordingly. The current size of FiberForm microscale geometry is relatively small (0.1mm $\times$0.1mm $\times$0.1mm). Implementing the model for a larger scale sample would correspond closely to reality. Furthermore, artificial geometry can produce a similar structure of Fiberform with a disorganized group of cylinder-shaped fibers, but the actual material properties still remain unknown, especially at different porosity values. Implementing both geometries into the model to extract the effective radiative properties can help truly com-

pared the structure and inspect the material properties at the same microscale level. The effect of fiber orientation, size, and sample porosity on radiative conductivity can also be thoroughly investigated in the future.

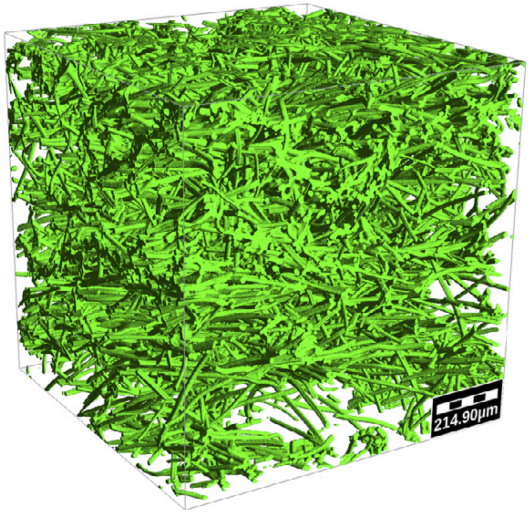

Figure 5.1: Micro-CT ray-tracing rendering of FiberForm [36]

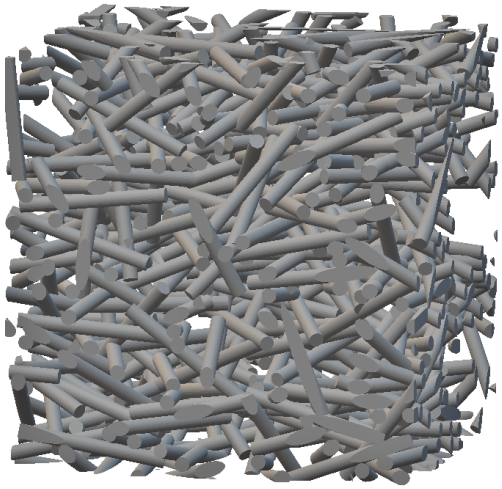

Figure 5.2: Example of FiberForm Created by OTTER [28]

Furthermore, the radiative conductivity can be combined with the solid and gas conductivity to provide the approximate total effective conductivity using a basic approach. For the gas conductivity. Qiao et al. [37] reported that for pores greater than $1.4\mu m$, the inherent conductivity of gas could be used, disregarding the reduction due to the Knudsen effect. Hence, the intrinsic conductivity of air [0.024 W/m-K] to the gas that is filling inside the pores can be used in the numerical model.

The solid conductivity of FiberForm was evaluated by Panerai et al. [35]. They used a 1 mm cubic sample of FiberForm and determined the value of the solid conductivity matrix in air standard conditions. With the solid and gas conductivity at the same microscale level, the total effective conductivity can be evaluated and possibly compared with experimental data.

2. **Radiation scattering**

   Only absorbing-emitting medium has been considered in the present model, and radiation scattering has been neglected. More realistically, molecules in participating media could reflect radiation in all directions. The type and amount of scattering depend on the size of the particles and the wavelength of the energy. To precisely determine the effect of participating media for a specific gas, spectrum dependency is also an important aspect. The equations can be formulated into spectrum dependence form and integrate over the range of wavelength. The attenuation factor for the gas at a specific wavelength can be found at the International Telecommunications Union (ITU) [39]. The data from ITU listed the estimate of gaseous attenuation by atmospheric gases for the frequency range from 1-1000 GHz.

3. **Combine radiation with conduction**

   Combined radiation and conduction heat transfer is important where semitransparent materials are used in high-temperature conditions, like fiber thermal protection systems. A common approach to the problem of combined radiation and conduction is based on the Rosseland approximation. However, the temperature distribution in the numerical model would most likely be different from the experiment measurement since conduction has been decoupled from the radiation during the convergent process. Including conduction during this transient process would produce a more realistic temperature distribution inside the fibers. Theoretically, this effect would be more imperative for the solid structure comparing to fibrous material, but the actual impact still needs more investigation. If the radiative equilibrium is not unique, combining solid conduction while iterating the surface temperature would produce a different temperature distribution and yield a different conductivity value.

Bibliography

[1] Aliasghar Ameri and James D. Felske. Radiation configuration factors for obliquely oriented finite length circular cylinders. *International Journal of Heat and Mass Transfer*, 25(5):728 – 736, 1982. doi:https://doi.org/10.1016/0017-9310(82)90180-6.

[2] Bertrand Baudouy. Heat transfer and cooling techniques at low temperature. *CAS-CERN Accelerator School: Superconductivity for Accelerators - Proceedings*, 01 2015. doi:10.5170/CERN-2014-005.329.

[3] William H. Bowman and Richard M. Lawrence. Space resource. ablative materials for high-temperature thermal protection of space vehicles. *Journal of Chemical Education*, 48(10):690, 10 1971. doi:10.1021/ed048p690. URL `https://doi.org/10.1021/ed048p690`.

[4] Thomas Burghardt. Final dragon 1 completes return to earth to conclude crs-20, April 2020. URL `https://www.nasaspaceflight.com/2020/04/final-dragon-1-return-earth/`.

[5] R.D. Cess. The interaction of thermal radiation with conduction and convection heat transfer11a portion of the work described herein was supported by the national science foundation through grant number g-19189. volume 1 of *Advances in Heat Transfer*, pages 1–50. Elsevier, 1964. doi:https://doi.org/10.1016/S0065-2717(08)70096-0. URL `https://www.sciencedirect.com/science/article/pii/S0065271708700960`.

[6] Douglas A. Codron, Brett A. Cruden, and Thanh Ho. *Emission Spectroscopy Characterization of Thermal Protection System Materials in Arc-Heated Flows.*

doi:10.2514/6.2014-2112. URL https://arc.aiaa.org/doi/abs/10.2514/6.2014-2112.

[7] T D Cooper and O O Srp. Refractory metals and their protection. *Aerospace Eng.*, 22(1), 1 1963.

[8] Miao CUI, Hai geng CHEN, and Xiao wei GAO. Mathematical models developed by zone method considering non-gray radiation properties of gas in combustion chamber. *Journal of Iron and Steel Research, International*, 17(11):13–18, 2010. ISSN 1006-706X. doi:https://doi.org/10.1016/S1006-706X(10)60163-X. URL https://www.sciencedirect.com/science/article/pii/S1006706X1060163X.

[9] Hadi Ebrahimi, Akbar Zamaniyan, Jafar S. Soltan Mohammadzadeh, and Ali Asghar Khalili. Zonal modeling of radiative heat transfer in industrial furnaces using simplified model for exchange area calculation. *Applied Mathematical Modelling*, 37(16):8004–8015, 2013. ISSN 0307-904X. doi:https://doi.org/10.1016/j.apm.2013.02.053. URL https://www.sciencedirect.com/science/article/pii/S0307904X13001923.

[10] E. R. G. Eckert. Radiative transfer, h. c. hottel and a. f. sarofim, mcgraw-hill book company, new york, 1967. 52 pages. *AIChE Journal*, 15(5):794–796, 1969. doi:10.1002/aic.690150504.

[11] Chao Fan, Xiao-Lei Li, Xin-Lin Xia, and Chuang Sun. Tomography-based pore level analysis of combined conductive-radiative heat transfer in an open-cell metallic foam. *International Journal of Heat and Mass Transfer*, 159:120122, 2020. ISSN 0017-9310. doi:https://doi.org/10.1016/j.ijheatmasstransfer.2020.120122. URL https://www.sciencedirect.com/science/article/pii/S0017931020330581.

[12] David E. Glass, Arthur D. Dilley, and H. Neale Kelly. Numerical analysis of convection / transpiration cooling. *Journal of Spacecraft and Rockets*, 38(1): 15–20, 2001. doi:10.2514/2.3666. URL https://doi.org/10.2514/2.3666.

[13] Tony Greicius. Nasa's stardust sample return was 10 years ago today, Jan 2016. URL https://www.nasa.gov/feature/nasas-stardust-sample-return-was-10-years-ago-today.

[14] Stefano Gulli, Luca Maddalena, and Serhat Hosder. *Integrated Analysis for the Design of Reusable TPS Based on Variable Transpiration Cooling for Hypersonic Cruise Vehicles*. 10th International Energy Conversion Engineering Conference, AIAA, 2012. doi:10.2514/6.2012-4161. URL https://arc.aiaa.org/doi/abs/10.2514/6.2012-4161.

[15] Jr. A. L. Crosbie H. F. Nelson, D. C. Look. Two-dimensional radiative backscattering from optically thick media. *J. Heat Transfer*, 1986.

[16] Max A. Heaslet and Robert F. Warming. Radiative transport and wall temperature slip in an absorbing planar medium. *International Journal of Heat and Mass Transfer*, 8(7):979 – 994, 1965. URL http://www.sciencedirect.com/science/article/pii/0017931065900839.

[17] M.A. Hossain, M.A. Alim, and D.A.S. Rees. The effect of radiation on free convection from a porous vertical plate. *International Journal of Heat and Mass Transfer*, 42(1):181–191, 1999. ISSN 0017-9310. doi:https://doi.org/10.1016/S0017-9310(98)00097-0. URL https://www.sciencedirect.com/science/article/pii/S0017931098000970.

[18] M.Anwar Hossain, Khalil Khanafer, and Kambiz Vafai. The effect of radiation on free convection flow of fluid with variable viscosity from a porous vertical plate. *International Journal of Thermal Sciences*, 40(2):115–124, 2001. ISSN

1290-0729. doi:https://doi.org/10.1016/S1290-0729(00)01200-X. URL https://www.sciencedirect.com/science/article/pii/S129007290001200X.

[19] H. C. Hottel and E. S. Cohen. Radiant heat exchange in a gas-filled enclosure: Allowance for nonuniformity of gas temperature. *AIChE Journal*, 4(1):3–14, 1958.

[20] Albert Huang. Low density ablators, May 2020. URL https://www.nasa.gov/centers/ames/thermal-protection-materials/tps-materials-development/low-density-ablators.html.

[21] Frank P Incropera and David P. DeWitt. *Fundamentals of Heat and Mass Transfer*. John Wiley Inc, 2002.

[22] Tingting Jing, Guoqiang He, Fei Qin, Wenqiang Li, Duo Zhang, and Pengkun Zhang. An innovative self-adaptive method for improving heat sink utilization efficiency of hydrocarbon fuel in regenerative thermal protection system of combined cycle engine. *Energy Conversion and Management*, 178:369 – 382, 2018. ISSN 0196-8904. doi:https://doi.org/10.1016/j.enconman.2018.10.038. URL http://www.sciencedirect.com/science/article/pii/S0196890418311397.

[23] Glenn Roberts Jr. The heat is on - x-rays reveal how simulated atmospheric entry conditions impact spacecraft shielding, 2017. URL https://newscenter.lbl.gov/2017/02/22/building-heat-shield-mars-mission.

[24] Sungwook Kang, J. Yoon Choi, and Sengkwan Choi. Mechanism of heat transfer through porous media of inorganic intumescent coating in cone calorimeter testing. *Polymers*, 11(2), 2019. ISSN 2073-4360. URL https://www.mdpi.com/2073-4360/11/2/221.

[25] Shuang Liu and Boming Zhang. Experimental study on a transpiration cooling thermal protection system. *Science China Technological Sciences*, 53:2765–2771, 10 2010. doi:10.1007/s11431-010-4055-8.

[26] Eugen Magyari and Asterios Pantokratoras. Note on the effect of thermal radiation in the linearized rosseland approximation on the heat transfer characteristics of various boundary layer flows. *International Communications in Heat and Mass Transfer*, 38(5):554–556, 2011. ISSN 0735-1933. doi:https://doi.org/10.1016/j.icheatmasstransfer.2011.03.006. URL https://www.sciencedirect.com/science/article/pii/S073519331100042X.

[27] Mustapha Malek, Nouh Izem, M. Shadi Mohamed, Mohammed Seaid, and Mohamed Wakrim. Numerical solution of rosseland model for transient thermal radiation in non-grey optically thick media using enriched basis functions. *Mathematics and Computers in Simulation*, 180:258–275, 2021. ISSN 0378-4754. doi:https://doi.org/10.1016/j.matcom.2020.08.024. URL https://www.sciencedirect.com/science/article/pii/S0378475420302913.

[28] Sean McDaniel, Mujan Seif, Rui Fu, Matthew Beck, and Alexandre Martin. *Development of Stochastic Model for Fibrous Ablators*. American Institute of Aeronautics and Astronautics, 2021/02/14 2021. doi:doi:10.2514/6.2021-1473. URL https://doi.org/10.2514/6.2021-1473.

[29] Miguel A.A. Mendes, Subhashis Ray, and Dimosthenis Trimis. A simple and efficient method for the evaluation of effective thermal conductivity of open-cell foam-like structures. *International Journal of Heat and Mass Transfer*, 66:412–422, 2013. ISSN 0017-9310. doi:https://doi.org/10.1016/j.ijheatmasstransfer.2013.07.032. URL https://www.sciencedirect.com/science/article/pii/S0017931013005863.

[30] Subhash C. Mishra and Manohar Prasad. Radiative heat transfer in participating

media —a review. *Sadhana*, 23(2):213, 1998. doi:10.1007/BF02745682. URL https://doi.org/10.1007/BF02745682.

[31] Nima Nouri. Radiative conductivity analysis of low-density fibrous materials. Master's thesis, University of Kentucky, 2015.

[32] Nima Nouri and Alexandre Martin. Three dimensional radiative heat transfer model for the evaluation of the anisotropic effective conductivity of fibrous materials. *International Journal of Heat and Mass Transfer*, 83:629–635, 2015. ISSN 0017-9310. doi:https://doi.org/10.1016/j.ijheatmasstransfer.2014.12.041. URL https://www.sciencedirect.com/science/article/pii/S0017931014011491.

[33] Nima Nouri, Francesco Panerai, Kaveh A. Tagavi, Nagi N. Mansour, and Alexandre Martin. Evaluation of the anisotropic radiative conductivity of a low-density carbon fiber material from realistic microscale imaging. *International Journal of Heat and Mass Transfer*, 95:535 – 539, 2016. ISSN 0017-9310. doi:https://doi.org/10.1016/j.ijheatmasstransfer.2015.12.004. URL http://www.sciencedirect.com/science/article/pii/S0017931015311236.

[34] Abdurrahman Ozturk. Implementation of view factor model and radiative heat transfer model in moose. Master's thesis, University of South Carolina, 2019.

[35] Francesco Panerai, Joseph Ferguson, Jean Lachaud, Alexandre Martin, Matthew J Gasch, and Nagi N Mansour. Analysis of fibrous felts for flexible ablators using synchrotron hard x-ray micro-tomography. *8th European Symposium on Aerothermodynamics for Space Vehicles, no. 89747, Lisbon, Portugal*, 2015.

[36] Francesco Panerai, Joseph C. Ferguson, Jean Lachaud, Alexandre Martin, Matthew J. Gasch, and Nagi N. Mansour. Micro-tomography

based analysis of thermal conductivity, diffusivity and oxidation behavior of rigid and flexible fibrous insulators. *International Journal of Heat and Mass Transfer*, 108:801–811, 2017. ISSN 0017-9310. doi:https://doi.org/10.1016/j.ijheatmasstransfer.2016.12.048. URL https://www.sciencedirect.com/science/article/pii/S0017931016327235.

[37] J. H. Qiao, R. Bolot, H. L. Liao, and C. Coddet. Knudsen effect on the estimation of the effective thermal conductivity of thermal barrier coatings. *Journal of Thermal Spray Technology*, 22(2):175–182, 2013. doi:10.1007/s11666-012-9878-3. URL https://doi.org/10.1007/s11666-012-9878-3.

[38] Svein Rosseland. *Astrophysik und atom-theoretische Grundlagen*, volume 11. Springer-Verlag, 1931. doi:https://doi.org/10.1007/978-3-662-26679-3.

[39] P Series. Attenuation by atmospheric gases. Febuary 2016. URL https://www.itu.int/dms_pubrec/itu-r/rec/p/R-REC-P.676-11-201609-I!!PDF-E.pdf.

[40] Robert Siegel. *Thermal radiation heat transfer*. Hemisphere Pub. Corp., 3rd ed. edition, 1992.

[41] M. Stackpoole, D. Kao, V. Qu, and G. Gonzáles. Post-flight evaluation of pica and pica-x - comparisons of the stardust src and space-x dragon 1 forebody heatshield materials. 2013.

[42] Eric C. Stern, Savio Poovathingal, Ioannis Nompelis, Thomas E. Schwartzentruber, and Graham V. Candler. Nonequilibrium flow through porous thermal protection materials, part i: Numerical methods. *Journal of Computational Physics*, 380:408–426, 2019. ISSN 0021-9991. doi:https://doi.org/10.1016/j.jcp.2017.09.011. URL https://www.sciencedirect.com/science/article/pii/S0021999117306708.

[43] M.A. Tahir, H. Vahedi Tafreshi, S.A. Hosseini, and B. Pourdeyhimi. Modeling the role of microstructural parameters in radiative heat transfer through disordered

fibrous media. *International Journal of Heat and Mass Transfer*, 53(21):4629 –4637, 2010. doi:https://doi.org/10.1016/j.ijheatmasstransfer.2010.06.030.

[44] A. J. Van Eekelen and J. Lachaud. Numerical validation of an effective radiation heat transfer model for fiber preforms. *Journal of Spacecraft and Rockets*, 48(3): 534–537, 2011. doi:10.2514/1.51865. URL `https://doi.org/10.2514/1.51865`.

[45] J. Vaniman, R. Fisher, C. Wojciechowski, and W. Dean. Ablative thermal protection systems. *NASA STI/Recon Technical Report A*, 83:576–583, July 1983.

[46] R. Viskanta and R.J. Grosh. Boundary layer in thermal radiation absorbing and emitting media. *International Journal of Heat and Mass Transfer*, 5(9):795–806, 1962. ISSN 0017-9310. doi:https://doi.org/10.1016/0017-9310(62)90180-1. URL `https://www.sciencedirect.com/science/article/pii/0017931062901801`.

[47] Frank M. White. *Heat Transfer*. Addison-Wesley, 1984.

[48] W. W. Yuen and E. E. Takara. Development of a generalized zonal method for analysis of radiative transfer in absorbing and anisotropically scattering media. *Numerical Heat Transfer, Part B: Fundamentals*, 25(1):75–96, 1994.

[49] Weijun ZHANG, Zhi YI, and Haigeng CHEN. A new simplified zonal method for furnace thermal radiation calculation based on imaginary planes. *Journal of Iron and Steel Research*, 21(4):419–426, 2014.

Vita

Mingping Zheng

Education

***Bachelor of Science* in Mechanical Engineering** 2015 – 2019

University of Kentucky,

Lexington, KY.

Publications

- Eytan Adler, Timothy Aiken, Cameron Byrd, Ethan Howell, Thomas McClure, James Nichols, Nicholas Bartel, Rayna Weibrecht and **Mingping Zheng**. "Subscale Demonstration and Validation of the Hercules Lunar and Mars Ascent, Descent, and Entry Vehicle," AIAA Scitech 2020 Forum. January 2020.

Presentations

- **Zheng, M.**, Nouri, N., and Martin, A., "Evaluation of the anisotropic radiative conductivity of fibrous material from realistic microscale imaging, 3rd Commonwealth Computational Summit, Lexington, Kentucky, October 2019.
- **Zheng, M.**, and Martin, A., "Evaluate Radiation conductivity of a fibrous material from microscale image," 45th AIAA Dayton-Cincinnati Aerospace Sciences Symposium, Dayton, Ohio, March 2020.